Measurement report: Vertical and temporal variability of near-surface ozone production rate and sensitivity in an urban area in Pearl River Delta (PRD) region, China

Jun Zhou[1,2#], Chunsheng Zhang[3#], Aiming Liu[3], Bin Yuan[1,2*], Yan Wang[1,2], Wenjie Wang[1,4], Jie-Ping Zhou[1,2], Yixin Hao[1,2], Xiao-Bing Li[1,2*], Xianjun He[1,2], Xin Song[1,2], Yubin Chen[1,2], Suxia Yang[1,2], Shuchun Yang[1,2], Yanfeng Wu[1,2], Bin Jiang[1,2], Shan Huang[1,2], Junwen Liu[1,2], Yuwen Peng[1,2], Jipeng Qi[1,2], Minhui Deng[1,2], Bowen Zhong[1,2], Yibo Huangfu[1,2], Min Shao[1,2*]

[1]College of Environment and Climate, Institute for Environmental and Climate Research, Jinan University, Guangzhou 511443, China

[2]College of Environment and Climate, Institute for Environmental and Climate Research, Guangdong-Hongkong-Macau Joint Laboratory of Collaborative Innovation for Environmental Quality, Guangzhou 511443, China

[3]Shenzhen National Climate Observatory, Shenzhen 518040, China

[4]Multiphase Chemistry Department, Max Planck Institute for Chemistry, Mainz 55128, Germany

[#]These authors contribute equally to this work.

Correspondence: Bin Yuan (byuan@jnu.edu.cn), Xiao-Bing Li (lixiaobing@jnu.edu.cn), Min Shao (mshao@jnu.edu.cn)

Abstract: Understanding the near-ground vertical and temporal photochemical O_3 formation mechanism is important to mitigate O_3 pollution. Here, we measured the vertical profiles of O_3 and its precursors at six different heights ranging from 5 to 335 m using a newly built vertical observation system in the Pearl River Delta (PRD) region, China. The net photochemical ozone production rate ($P(O_3)_{net}$) and O_3 formation sensitivities at various heights were diagnosed using an observation-based model coupled with the Master Chemical Mechanism (MCM v3.3.1). Moreover, to assess model performance and identify the causative factors behind O_3 pollution episodes, the $P(O_3)_{net}$ was measured at 5 m ground level utilizing a custom-built detection system. In total three O_3 pollution episodes and two non-episodes were captured. The identified

O_3 pollution episodes were found to be jointly influenced by both photochemical production and physical transport, with local photochemical reactions playing a major role. The high index of agreement (IOA) calculated from comparing the modelled and measured $P(O_3)_{net}$ values indicated the rationality to investigate the vertical and temporal variability of O_3 formation mechanisms using modelling results. However, the measured $P(O_3)_{net}$ values were generally higher than the modelled $P(O_3)_{net}$ values, particularly under high NOx conditions, which may indicate a potential underestimation of total RO_2 by the model. Throughout the measurement period, the contribution of different reaction pathways to O_3 production remained consistent across various heights, with HO_2+NO as the major O_3 production pathway, followed by RO_2+NO. We observed $P(O_3)_{net}$ decreasing with the increase in measurement height, primarily attributed to the decreased O_3 precursors anthropogenic volatile organic compounds (AVOC) and oxygenated volatile organic compounds (OVOC). O_3 formation regimes were similar at different heights during both episodes and non-episodes, either located in the volatile organic compounds (VOCs) sensitive regime or in the transition regime and more sensitive to VOCs. Diurnally, photochemical O_3 formation typically remained in the VOCs sensitive regime during the morning and noon, but transitioned to the transition regime and more sensitive to VOCs in the afternoon around 16:00 local time (LT). The vertical and temporal O_3 formation is most sensitive to OVOC, suggesting that targeting specific VOCs for control measures is more practical and feasible at the observation site. The vertical temporal analysis of O_3 formation mechanisms near the ground surface in this study provides critical foundational knowledge for formulating effective short-term emergency and long-term strategies to combat O_3 pollution in the PRD region of China.

1. Introduction

Tropospheric ozone (O_3), which has adverse effects on ecosystems, climate change, and human health (Fiore et al., 2009; Anenberg Susan et al., 2012; Seinfeld, 2016), has become an important factor resulting in severe regional air pollution in China (Zhu et al., 2020). Tropospheric O_3 mainly comes from stratospheric intrusions and the photochemical reactions of O_3 precursors, involving volatile organic compounds (VOCs) and nitrogen oxides (NOx=NO+NO_2). The O_3-precursor relationship can be split into a "NOx-limited" or "VOC-limited" or "mixed-sensitive" regime (Seinfeld and Pandis, 2016; Sillman S., 1999). A "NOx-limited" regime has higher VOCs/NOx ratios

and the O_3 formation is sensitive to NOx concentration changes, while a "VOCs-limited" regime has lower VOCs/NOx ratios and the O_3 formation decreases with increasing NO_X and increases with increasing VOCs. In a "mixed-sensitive" regime, O_3 formation responds positively to changes in both NOx and VOC emissions (Wang et al., 2019). Local O_3 concentrations can be further influenced by meteorological conditions and the regional transport of O_3 and its precursors (Gong and Liao, 2019; Chang et al., 2019). The Pearl River Delta (PRD) stands out as one of the most rapidly developing economic and urbanized regions in China, which currently is suffering from severe ground-level O_3 pollution (Lu et al., 2018; Yang et al., 2019). Currently, many scholars have analyzed the relationship between tropospheric O_3 pollution and its precursors and meteorological elements in the PRD region, results show that the surface O_3 pollution is determined by both local photochemistry and physical transport, with long-range transport contributing 30%-70% to surface O_3 concentrations (Mao et al., 2022; Shen et al., 2021; Li et al., 2012, 2013). However, the distribution of O_3 is highly variable at different altitudes (Wang et al., 2021), due to vertical differences in VOC concentrations and sources, as well as the sensitivity of O_3 formation (Liu et al., 2023; Tang et al., 2017). Due to the presence of strong vertical mixing driven by the surface heating effect in the daytime boundary layer, the budget of the O_3 at the ground level and also at an arbitrary height in the daytime boundary layer is closely related to the formation and removal of O_3 at other heights (Tang et al., 2017). In addition, the difference in vertical gradients of precursors may drive the vertical change in the photochemical formation regimes of O_3 (Zhao et al., 2019). Using data from only one height to understand the photochemical reactions in the planetary boundary layer is of great limitation. Thus, diagnosing the O_3 formation mechanism at different heights is essential to achieve effective control of O_3 pollution.

Currently, remote sensing techniques with high time resolution and real-time response, such as lidar and optical absorption spectroscopy, have been utilized to measure the vertical distribution of O_3 (Luo et al., 2020a; Wang et al., 2021). However, in situ measurements of VOCs at various heights primarily rely on offline methods combined with diverse techniques, including aircraft, tethered balloons, tall buildings and towers, unmanned aerial vehicles (UAVs or drones), and satellite observations (Klein et al., 2019; Li et al., 2022; Geng et al., 2020; Benish et al., 2020; Li et al., 2021; Wang et al., 2019). Owing to the low time resolution of these monitoring techniques,

achieving continuous vertical coverage of VOCs and NOx measurements is challenging. Consequently, the vertical distribution structure of VOCs remains unclear, thus largely hindering our understanding of the vertical and temporal regional O_3 formation mechanism.

To fill the gaps in the existing studies, we utilized a newly constructed vertical observation system based on the Shenzhen Meteorological Gradient Tower (SZMGT) (Li et al., 2023). This system measured the vertical profiles of O_3 and its precursors at six different heights from 5 to 335 m. To diagnose the net O_3 production rate, $P(O_3)_{net}$, and O_3 formation sensitivities across various heights, we employed an observation-based model coupled with the Master Chemical Mechanism (MCM v3.3.1), referred to as OBM-MCM in the following. Additionally, we employed a novel net photochemical O_3 production rate ($P(O_3)_{net}$, NPOPR) detection system to measure the $P(O_3)_{net}$ at the 5 m ground level to explore potential reasons for O_3 pollution episodes (Hao et al., 2023), i.e., examine the contribution of chemical and physical processes to changes in O_3 concentration. Comparisons between the directly measured $P(O_3)_{net}$ results and the model-derived data enabled us to evaluate the simulation accuracy and explore potential reasons for discrepancies of the OBM-MCM model concerning photochemical O_3 formation. Based on these results, we have extensively discussed the vertical and temporal variability in $P(O_3)_{net}$ and O_3 formation sensitivity, while acknowledging potential biases associated to the modelling. The findings of this study offer a new benchmark for understanding the vertical profile of photochemical O_3 formation mechanism, aiding in the identification of the primary driver of ground-level O_3 pollution. This identification is crucial as it can provide essential theoretical support for developing short-term effective emergency and long-term control measures targeting O_3 in PRD region of China.

2. Materials and Methods

2.1 Sampling site

Field measurements were conducted at the Shenzhen Meteorological Gradient Tower (SZMGT) (22.65° N,113.89° E) from November 13 to December 10, 2021. The SZMGT is 365 m high and is currently the tallest mast tower in Asia and the second tallest of this kind in the world. The main structure of the tower is made of steel, steel stray lines are used for fixing and securing the tower. It is located in the Tiegang

Reservior Water Reserve at Bao'an District of Shenzhen, in the Pearl River Delta (PRD) region of China. The area is surrounded by a high density of vegetation, reservoir features, low-rise buildings, and hills/mountains (Luo et al., 2020b).

2.2 Instrumentation

2.2.1 The vertical sampling system

A tower-based observation system for traces gases using long perfluoroalkoxy alkane (PFA) tubing (OD: 1/2") was used to sample the O_3 and O_3 precursors at six heights during the campaign, including 5, 40, 70, 120, 220, and 335 m above the ground. All six tubes were continuously drawn using a rotary vane vacuum pump to keep flushing with ambient air to reduce tube delay of the organic compounds, with the flow rate controlled by critical orifices (orifice diameter: 0.063"). A Teflon solenoid valve group was used to switch the air samples at specified time intervals so that the subsamples from these six heights could be sequentially drawn by instruments (see Fig. S1). Consequently, the flow rates of the air sample streams for the six tubes varied between 12.0 and 15.0 SLPM without subsampling and were less than 20 SLPM with subsampling. The residence time of the sample gas in the longest tube (~ 400 m) is less than 180 s at a flow rate of 13 SLPM. The impacts of long tubing on measurements of various of trace gases, including O_3, NOx, and a set of organic compounds, were systematically investigated using a combination of laboratory tests, field experiments, and modelling techniques. Field observations proved that this observation system is suitable for analyzing spatio-temporal variations of atmospheric trace gases, with many trace gases could be well measured. More details about the establishment and the characterization of this observation system are described elsewhere (Li et al., 2023).

2.2.2 $P(O_3)_{net}$ measurement

During the campaign, the $P(O_3)_{net}$ at the 5 m ground level was measured using the home-made NPOPR detection system, which was built based on the dual-channel reaction chambers technique. The improvement, characterization, and the photochemical O_3 formation mechanism in the reaction and reference chambers of the NPOPR detection system are described in our previous study (Hao et al., 2023). Briefly, the NPOPR detection system consists of reaction and reference chambers with the same geometry and made of quartz glass. The length and inner diameter of the quartz glass cylinder are 700 mm and 190.5 mm, respectively, which resulted in an inner volume of

~ 20 L. The outer surface of the reference chamber was covered with an Ultem film (SH2CLAR, 3 M, Japan) for ultraviolet (UV) protection, which can block sunlight with wavelengths < 390 nm, thus preventing photochemical reactions inside. During the experiment, both the reaction and reference chambers were placed outdoors and directly exposed to sunlight to simulate real ambient photochemical reactions. Ambient air was introduced into the reaction and reference chambers at the same flow rate, and a Teflon filter was mounted before the chamber inlet to remove fine particles. To correct for the effect of fresh NO titration to O_3, we use O_X (=O_3+NO_2) instead of O_3 to quantify the O_3 generated by photochemical reactions (Pan et al., 2015; Tan et al., 2018). A stream of air from the two chambers was alternately introduced into an NO-reaction chamber every 2 min to convert O_3 in the air to NO_2 in the presence of high concentrations of NO (O_3+NO→NO_2), and the Ox concentrations from the outlet NO-reaction chamber, i.e., the total NO_2 concentrations including the inherent NO_2 in the ambient and that converted from O_3, were measured by a Cavity Attenuated Phase Shift (CAPS) NO_2 Monitor (Aerodyne research, Inc., Billerica MA, USA) to avoid other nitrogen oxide interferences to the NO_2 measurement (such as alkyl nitrates, peroxyacyl nitrates, peroxynitric acid, nitrogen pentoxide, etc.). $P(O_3)_{net}$ was obtained by dividing the difference between the Ox concentrations in the reaction and reference chambers (ΔOx) by the mean residence time of air in the reaction chamber $\langle\tau\rangle$:

$$P(O_3)_{net} = P(O_X)_{net} = \frac{\Delta O_x}{\tau} = \frac{[O_x]_{reaction} - [O_x]_{reference}}{\tau} \quad (1)$$

A schematic of the NPOPR detection system is shown in Fig. S2. The pulse experiments were performed to quantify the residence time in the chambers (Hao et al., 2023).

[Ox] values plugged in Eq. (1) to derive $P(O_3)_{net}$ are measured values corrected for wall losses of Ox and the light-enhanced loss of O_3 ($d[O_3]$) in the reaction and reference chambers during daytime (Hao et al., 2013):

$$\gamma = \frac{d[O_3] \times D}{\omega \times [O_3] \times \tau} \quad (2)$$

where γ is the light-enhanced loss coefficient of O_3, which is derived from $J(O^1D)$ according to the relationship obtained from the outdoor experiments (for more details, see supplementary materials: Sect. S3). $d[O_3]$ represents the difference between the O_3

mixing ratios at the inlet and outlet of the reaction and reference chambers, D is the diameter of the chambers, ω is the average velocity of O_3 molecules, [O_3] is the injected O_3 mixing ratio at the inlet of the reaction and reference chambers, and τ is the average residence time of the air in the reaction and reference chambers. When quantifying the light-enhanced O_3 loss (d[O_3]) during the ambient air measurement, we first calculate γ using the measured $J(O^1D)$ and the γ -$J(O^1D)$ equations listed in Fig. S8 in the reaction and reference chambers, then use the measured [O_3] and Eq. (2) to calculate d[O_3]. The results show that such kind of correction can increase the measured $P(O_3)_{net}$ by 10% (25% percentile) to 24% (75% percentile), with a median of 17%.

The limit of detection (LOD) of the NPOPR detection system is 2.3 ppbv h^{-1} at the sampling air flow rate of 5 L min^{-1}, which is obtained as three times the measurement error of $P(O_3)_{net}$ (Hao et al., 2013). The measurement error of $P(O_3)_{net}$ is determined by the estimation error of Ox in the reaction and reference chambers, which includes the measurement error associated with the O_X of the CAPS-NO_2 monitor and the error due to the light-enhanced loss of O_3. This collective measurement error is referred to as the measurement precision of the NPOPR detection system, with further details provided in the supplementary materials, specifically in Sect. S4. The measurement accuracy of the NPOPR detection system is determined as 13.9 %, representing the maximum systematic error resulting from photochemical O_3 production in the reference chamber. Our earlier research indicated that the modelled $P(O_3)_{net}$ in the reaction chamber is similar to that modelled in ambient air, with the modelled $P(O_3)_{net}$ in the reference chamber accounting for 0-13.9% of that in the reaction chamber (Hao et al., 2023). This is due to the UV protection Ultem film covered on the reference chamber, which only filtered out the sunlight with wavelengths < 390 nm, allowing photochemical O_3 production to persist at the sunlight wavelength between 390 nm and 790 nm. Here, we have utilized the same modelling approach described in Hao et al. (2013) to quantify the $P(O_3)_{net}$ in the reference chamber and corrected for the bias introduced by the measurement accuracy.

2.2.3 VOCs measurement

VOCs were measured using a high-resolution proton transfer reaction time-of-flight mass spectrometer (PTR-TOF-MS, Ionicon Analytik, Austria) (Wang et al., 2020a; Wu et al., 2020) and an off-line gas chromatography mass spectrometry flame

ionization detector (GC-MS-FID) (Wuhan Tianlong, Co. Ltd, China) (Yuan et al., 2012). The concentrations of oxygenated VOCs (OVOC), including formaldehyde (HCHO) and acetaldehyde (CH_3CHO), were measured via PTR-TOF-MS, and the non-methane hydrocarbons (NMHC) were measured via GC-MS-FID. PTR-TOF-MS was run with both hydronium ion (H_3O^+) (Yuan et al., 2017; Wu et al., 2020) and nitric oxide ion (NO^+) (Wang et al., 2020) modes. The measurement error of PTR-TOF-MS was lower than 20%, more details of the PTR-TOF-MS technique can be found in our previous publication (Yuan et al., 2017). The H_3O^+ and NO^+ modes were automatically switched with 20 min H_3O^+ mode and 10 min NO^+ mode. The background signal of each mode was measured every 30 min for at least 2 min by automatically switching the ambient measurement to a custom-built platinum catalytic converter heated to 365 ^oC. Operating the PTR-ToF-MS instrument in NO^+ mode primarily detects higher alkanes, which are known significantly contribute to the formation of secondary organic aerosols (SOA) but negligible contributions to photochemical O_3 formation (Wang et al., 2020). Eventually, we only used VOCs measured during the H_3O^+ mode, which was operated at a drift tube pressure of 3.8 mbar, a temperature of 120 ^oC, and a voltage of 760 V, resulting in an E/N (E refers to the electric field and N refers to the number density of the buffer gas in the drift tube) value of ~ 120 Td (townsend). 3035 ions with m/z up to 510 were obtained at time resolutions of 10 s. A gas standard with 35 VOC species was used for calibrations of the PTR-ToF-MS once per day. Raw data from PTR-TOF-MS were analyzed using Tofware software (Tofwerk AG, v3.0.3). Due to the humidity dependencies of various VOCs signals of the PTR-ToF-MS observed in laboratory studies, such as formaldehyde, benzene, methanol, ethanol, and furan (Wu et al., 2020), we determined their humidity-dependence curves. During data analysis, we removed the impacts of ambient humidity change on the measured signals of the PTR-ToF-MS according to these humidity-dependence curves. For the off-line GC-MS-FID measurement, whole-air samples were collected using 3.2 L electro-polished stainless-steel canisters (Entech, USA) at 5 and 120 m at time intervals of two hours. Two automatic canister samplers connected to 12 canisters were used to collect the whole-air samples, with each of canister collecting the sample for 10 min. The canisters were analyzed within one week (Zhu et al., 2018). The concentrations of 56 NMHC species in the canister were analyzed by GC-MS/FID which was calibrated daily using the mixture of a photochemical assessment monitoring stations (PAMS) standard gas and pure N_2. In addition, the mixture of PAMS standard gas and pure N_2 with species

concentrations of 1 ppbv was injected into the analytical system every 10 samples to check the operational stability of the instrument. Pure N_2 was injected into the analytical system at the start and end of each day's analysis to provide reference blank measurements. A full list of all 56 non-methane hydrocarbons (NMHCs) can be found in the supplementary material (Table S2).

2.2.4 Other parameters

The photolysis frequencies of different species were measured using the actinic flux spectrometer (PFS-100, Focused Photonics Inc, China). O_3, CO, and NO_X concentrations were measured by a 2B O_3 monitor based on dual-channel UV-absorption (Model 205, 2B Technologies, USA), a gas filter correlation (GFC) CO analyzer (Model 48i, Thermo Fisher Scientific, USA), and a chemiluminescence NOx monitor (Model 42i, Thermo Fisher Scientific, USA), respectively. According to our test (Zhou et al., 2025), a 5% overestimation could be caused in the NO_2 measurement using the chemiluminescence technique compared to the CAPS technique, due to some NO_Z species (i.e., HNO_3, peroxyacetyl nitrate (PANs), HONO, etc.)(Dunlea et al., 2007), this will result in a decrease of the modelled $P(O_3)_{net}$ by < 4%, which is negligible compared to the bias caused by the $P(O_3)_{net}$ in the reference chamber (~ 14%) (Zhou et al., 2023).Temperature (*T*), relative humidity (RH), and pressure (*P*) were measured by a portable weather station (Met Pak, Gill Instruments Ltd, UK).

2.3 Data analysis

2.3.1 Observation-based chemical box model

We investigated the detailed photochemical O_3 formation mechanism during the observation period based on the field observed data. The specific tropospheric O_3 photochemical formation process involves the photolysis of NO_2 at < 420 nm (Sadanaga et al., 2017). Simultaneously, RO_X (RO_X=OH+HO_2 +RO_2) radical cycles provide HO_2 and RO_2 to oxidize NO to NO_2, resulting in the accumulation of O_3 (Shen et al., 2021; Cazorla and Brune, 2010; Sadanaga et al., 2017). Therefore, the ROx radicals and the O_3, OH, NO_3 oxidants play important roles in photochemical O_3 formation. A zero-dimensional box model based on the Framework for 0-D Atmospheric Modelling (F0AM) v3.2 (Wolfe et al., 2016) coupled with the MCM v3.3.1 was used to simulate the $P(O_3)_{net}$. MCM v3.1.1 contains a total of 143 VOCs, more than 6700 species, involving more than 17000 reactions (Jenkin et al., 2015).

$P(O_3)_{net}$ and O_3 concentrations were simulated by constraining *T*, RH, *P*, organic and inorganic substances in gases, including 12 OVOCs (methanol, ethanol, formaldehyde, acetaldehyde, acrolein, acetone, hydroxyacetone, phenol, *m*-cresol, methyl vinyl ketone, methacrylaldehyde, methyl ethyl ketone), 56 NMHCs (toluene, benzene, isoprene, styrene, etc. as listed in Table S2), inorganic gaseous pollutants (O_3, NO, NO_2, and CO), and photolysis rate values ($J(O^1D)$, $J(NO_2)$, $J(H_2O_2)$, J(HONO), J(HCHO_M), J(HCHO_R), $J(NO_3\_M)$, $J(NO_3\_R)$, etc.). The VOCs, NOx, *T*, RH and *P* were constrained throughout the modelling period, while O_3 was not constrained after providing initial concentration values. To avoid the build-up of long-lived species to unreasonable levels, we also considered the physical dilution process by setting a constant dilution factor of 1/43200 s^{-1} throughout the modelling period (Liu et al., 2021; Decker et al., 2019). Additionally, the dry deposition rate of O_3 was set to 0.42 cm s^{-1}, and the background of O_3, CO, and CH_4 were set to 30, 70, and 1800 ppbv, respectively, based on the findings of Wang et al. (2011), Wang et al. (2022a), and WMO greenhouse gas bulletin (2022). The model was run in a time-dependent mode with a resolution of 5 min, and it was run for spin-up time of 72 h to establish steady-state concentrations for secondary pollutants that were not constrained during the simulation. $P(O_3)_{net}$ can be expressed by the difference between O_3 production rate ($P(O_3)$) and O_3 destruction rate ($D(O_3)$), where $P(O_3)$ and $D(O_3)$ can be calculated as Eq. (3)-(4):

$$P(O_3) = k_{HO_2+NO}[HO_2][NO] + \sum_i k_{RO_{2,i}+NO}[RO_{2i}][NO]\varphi_i \quad (3)$$

$$D(O_3) = k_{O(^1D)+H_2O}[O(^1D)][H_2O] + k_{OH+O_3}[OH][O_3] + k_{HO_2+O_3}[HO_2][O_3] + k_{O_3+alkenes}[O_3][alkenes] + k_{OH+NO_2}[OH][NO_2] + k_{RO_{2,i}+NO_2}[RO_{2i}][NO_2] \quad (4)$$

where k_{M+N} represents the bimolecular reaction rate constant of M and N, the subscript '*i*' refers to different types of RO_2, and φ_i is the yield of NO_2 of the reaction RO_{2i}+NO. The relevant reaction rates of $P(O_3)$ and $D(O_3)$ and the mean measured concentrations of each VOC category at 5 m ground during O_3 episodes and non-episodes used in the model are listed in Tables S1 and S2.

2.3.2 Derive contribution of chemical and physical processes to O3 changes on the ground level

It is known that chemical and physical processes jointly influence the O_3

concentration changes near the ground surface (Xue et al., 2014; Tan et al., 2019). The direct measurement of $P(O_3)_{net}$ gave us a chance to identify the contribution of chemical and physical processes to the variation of observed O_3 concentrations using the following equation:

$$\frac{dO_X}{dt} = P(O_X)_{net} + R(O_X)_{trans} \quad (5)$$

Where $\frac{dO_X}{dt}$ is the change rate of the observed O_x mixing ratio change (ppbv h^{-1}), $P(Ox)_{net}$ denotes the net photochemical O_3 production rate (ppbv h^{-1}), which was equal to $P(O_3)_{net}$ and measured directly by the NPOPR system. $R(O_X)_{trans}$ represents O_3 mixing ratio change due to physical transportation (ppbv h^{-1}), including the horizontal and vertical transport, dry deposition and the atmospheric mixing (Liu et al., 2022). To correct the effects of NO titration to O_3, we have replaced O_3 with O_X (=O_3+NO_2) during the calculation in this study (Pan et al., 2015).

2.3.3 Model performance

In order to judge the reliability of the model simulation, we calculated the index of agreement (IOA) based on the measured and modelled $P(O_3)_{net}$ and O_3 at 5 m above the ground level using the following equation (Liu et al., 2019):

$$\mathrm{IOA} = 1 - \frac{\sum_{i=1}^{n}(O_i - S_i)^2}{\sum_{i=1}^{n}(|O_i - \bar{O}| - |S_i - \bar{O}|)^2} \quad (6)$$

Where S_i and O_i represents the simulated and observed $P(O_3)_{net}$ or O_3 values at the same time, respectively, $\bar{O}$ is the averaged observed value, and n is the data number. Furthermore, we also judged the model simulation performance using statistical measures, including the normalized mean bias (NMB) and normalized mean error (NME), which are defined as:

$$\mathrm{NMB} = \frac{\sum_{i=1}^{n}(S_i - O_i)}{\sum_{i=1}^{n} O_i} \cdot 100\ \% \quad (7)$$

$$\mathrm{NME} = \frac{\sum_{i=1}^{n}|S_i - O_i|}{\sum_{i=1}^{n} O_i} \cdot 100\ \% \quad (8)$$

Where S_i and O_i have the same meaning as Eq. (6), and n is the total number of such data pairs of interest. The results will be discussed in Sect. 3.2.2.

2.3.4 OH reactivity

In order to investigate the influence of the photochemical reactions of different VOCs to photochemical O_3 formation, we calculated the OH reactivities of different VOCs, which is the sum of concentrations of OH reactants multiplied by their reaction rate coefficients, as shown below:

$$k_{\mathrm{OH}} = k_i \times [\mathrm{VOCs}]_i \quad (9)$$

where k_{OH} represents the total OH reactivity of a group of VOCs species, k_i represents the rate constants between OH radicals and different VOCs species i, $[\mathrm{VOCs}]_i$ represents the concentration of species i. In this study, we summarized the OH reactivities of different kinds of VOCs groups together to investigate their influence on the vertical gradient $P(O_3)_{net}$ in Sect. 3.2.3.

2.3.5 O_3 formation potential

The O_3 formation potential is calculated using the product of the VOC concentration and the maximum incremental reactivity (MIR) coefficient (dimensionless, gram of O_3 produced per gram of VOCs) (Carter et al., 2012):

$$\mathrm{OFP}_i = \sum_i [\mathrm{VOC}]_i \times \mathrm{MIR}_i \quad (10)$$

Where OFP_i is the O_3 formation potential of species i, $[\mathrm{VOC}]_i$ is the mass concentration or emission of species i, and MIR_i denotes the maximum increment reactivity of species i (g O_3/g VOCs).

2.3.6 O_3 formation regime

The sensitivity of photochemical O_3 production to its precursors was diagnosed by calculating the relative incremental reactivity (RIR) using the OBM-MCM model. RIR is defined as the percent change in O_3 photochemical production per percent change in the concentration of its single precursor/precursor group (Cardelino and Chameides, 1995). Therefore, the RIR for precursor (group) X can be expressed as:

$$RIR = \frac{\Delta P(O_3)/P(O_3)}{\Delta X/X} \quad (11)$$

where the $\Delta X/X$ represent the percent change in different O_3 precursors or precursor groups. We classified the measured VOCs into anthropogenic organic compounds (AVOC), biogenic organic compounds (BVOC), and OVOC group, and investigated the O_3 formation sensitivity to these different types of VOCs.

3. Results and discussions

3.1 Vertical and temporal profile of O_3 and its precursors

3.1.1 O_3 and its precursors at 5 m ground level

Figure 1 shows the time series of the major trace gases, photolysis rate constants, and meteorological parameters at 5 m ground-level during the observation period at SZMGT. Over the 1-month field observation period, a total of 3 O_3 pollution episodes (referred to episodes hereafter) and 2 non-O_3 pollution episodes (referred to non-episodes hereafter) were captured. O_3 pollution episodes were defined as the days during which the hourly average O_3 concentration at ground-level (5 m) exceed the Grade II standard (102 ppbv, GB 3095-2012, China; Ambient Air Quality Standards, 2012), while the remaining days were defined as non-episodes. Episode days (marked as gray columns in Fig. 1) included November 13-18 (episode I), November 26 (episode II), and December 7-9 (episode III), while the non-episode days included November 22-25 (non-episode I), November 26-27 and 30 (non-episode II). The corresponding daytime mean values (6:00-18:00 LT) during all episode days and non-episode days are shown in Table 1. During the daytime of episode days (episodes I, II, and III), the mean concentrations of O_3 were 70.1±28.6, 59.5±32.4, and 71.3±31.0, respectively. The mean *T* and RH were 22.3±2.5 ℃ and 56.2±14.5 % for episode I, 20.4±3.2 ℃ and 52.2±16.7 % for episode II, and 20.6±3.4 ℃ and 58.2±17.2 % for episode III. During non-episode days, the mean concentrations of O_3 were 45.3±16.2 and 63.7±21.3 ppbv for non-episode I and II, respectively. The corresponding mean *T* and RH were 18.4±4.3 ℃ and 69.5±15.4 % for non-episode I, and 21.3±2.7 ℃ and 51.8 ±13.7 % for non-episode II. These observations indicate that the *T* and RH during episode days were not significantly different from those during non-episode days. This phenomenon contrasts with previous studies in the PRD area, where O_3 pollution episodes were generally associated with high *T* and low RH (Mousavinezhad et al., 2021; Hong et al., 2022).

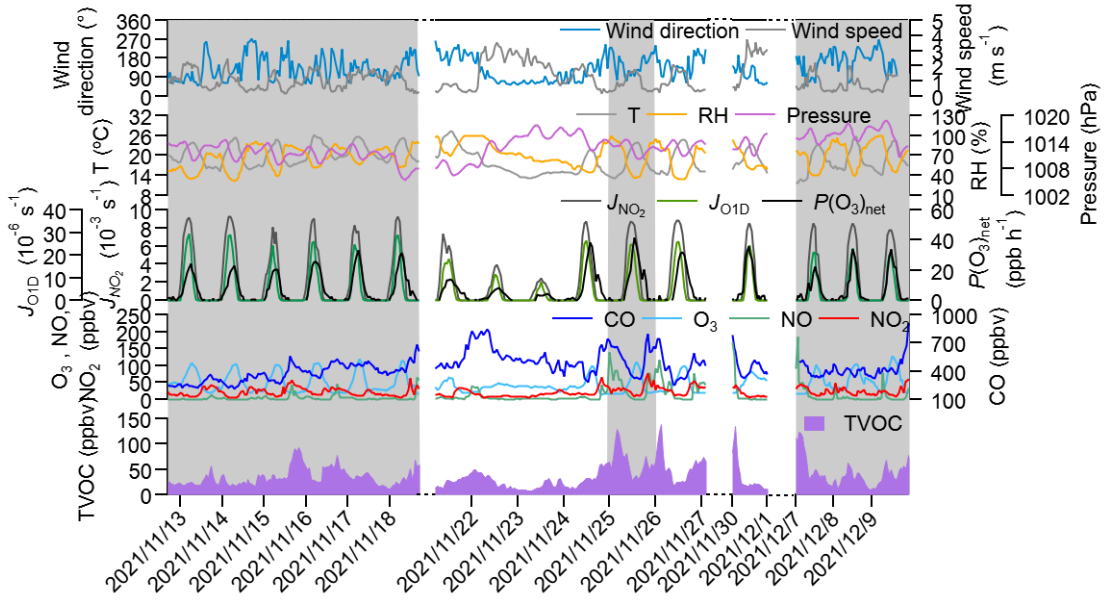

403

404 **Figure 1. Time series of major trace gases, photolysis rate constants, and meteorological**
405 **parameters at 5 m ground level during the observation period. The gray columns show the**
406 **typical O_3 episodes that occurred.**

407 **Table 1. Daytime major trace gases concentrations (units: ppbv), $P(O_3)_{net}$ (units: ppbv h^{-1}),**
408 **and meteorological parameters during different episodes and non-episodes during the**
409 **observation period (from 13 November to 9 December 2021) at SZMGT.**

Parameters	Mean±SD				
	Episode I	Episode II	Episode III	Non-episode I	Non-episode II
O_3	70.1±28.6	59.5±32.4	71.3±31.0	45.3±16.2	63.7±21.3
TVOC	29.6±10.6	53.8±21.7	42.9±11.5	23.3±8.6	26.8±11.1
CO	344.9±85.1	408.8±85.4	397.2±42.1	508.5±117.2	383.4±74.6
NO	2.3±2.6	13.1±17.4	6.6±13.8	2.9±2.0	6.8±13.1
NO_2	15.6±7.5	22.3±10.2	20.0±8.3	14.1±6.8	15.4±8.8
OFP (g m^{-3})	5.1E-4± 7.5E-5	1.0E-3± 2.0E-4	7.2E-4± 8.3E-5	4.1E-4± 5.6E-5	4.7E-4± 7.8E-5
$P(O_3)_{net}$* ppbv h^{-1})	14.3±10.7	21.5±14.9	14.6±11.9	5.6±4.6	18.9±13.9
T (°C)	22.3±2.5	20.4±3.2	20.6±3.4	18.4±4.3	21.3±2.7
RH (%)	56.2±14.5	52.2±16.7	58.2±17.2	69.5±15.4	51.8±13.7
Wind speed (m s^{-1})	1.3±0.5	1.2±0.4	1.1±0.5	1.8±0.9	2.1±0.9
wind direction (°)	115.5±48.7	128.6±35.3	144.8±57.1	115.0±57.6	115.3±36.2

410 * All values here were calculated as the mean average values during daytime (6:00-18:00 LT).

411 The mean concentrations of O_3 precursors, including CO, NO, NO_2, and the total

VOCs measured by PTR-TOF-MS (shown as TVOC in Fig. 1 and Table 1), did not exhibit notable discrepancies between episodes and non-episodes. This suggests that their concentrations during O_3 pollution episodes can vary, being either higher or lower than those observed during non-episodes (as shown in Table 1). For example, though there are days with very high hourly average O_3 concentrations which define O_3 pollution episodes-where levels exceed the Grade II standard of 102 ppbv-the overall average O_3 concentrations for episode II is not higher than that of non-episode II. This suggests that despite the occurrence of peak hourly levels, the average concentration for episode II remains lower, highlighting the fluctuating pattern of O_3 levels during these episodes. Further comparison of the daytime mean O_3 formation potential (OFP) and the measured $P(O_3)_{net}$ during episodes and non-episodes showed no significant differences, ranging from 5.1×10^{-4} to 1.0×10^{-3} g m^{-3} and 14.3 to 21.5 ppb h^{-1}, respectively, during non-episodes, whereas they are ranged from 4.1×10^{-4} to 4.7×10^{-4} g m^{-3} and 5.6 to 18.9 ppb h^{-1} respectively, during episodes. Although OFP was always higher during episodes than during non-episodes, the mean $P(O_3)_{net}$ values during episodes I and III were even lower than during non-episodes II. The higher O_3 concentrations may be due to the more stable weather conditions during episodes I and III (with lower wind speed), which benefits the accumulation of O_3 formed by local photochemical O_3 formation. While for non-episode II, even it processes higher $P(O_3)_{net,}$ the outflow of O_3 from the observation site by physical processes may be higher due to the higher wind speed. These findings indicate that the O_3 pollution episodes stem from either substantially elevated local photochemical O_3 formation (i.e., episode II), or the accumulation of O_3 formed by moderate local photochemical O_3 formation under stable weather conditions (i.e., episodes I and II). Notably, when local photochemical reactions contribute intensely to the formation of O_3, favorable weather conditions facilitating O_3 outflow diminish the likelihood of O_3 pollution occurrences (i.e., non-episode II). These results indicate that O_3 pollution episodes are jointly affected by the photochemical reactions and physical transport processes, which we will discuss in more detail in Sect. 3.2.1.

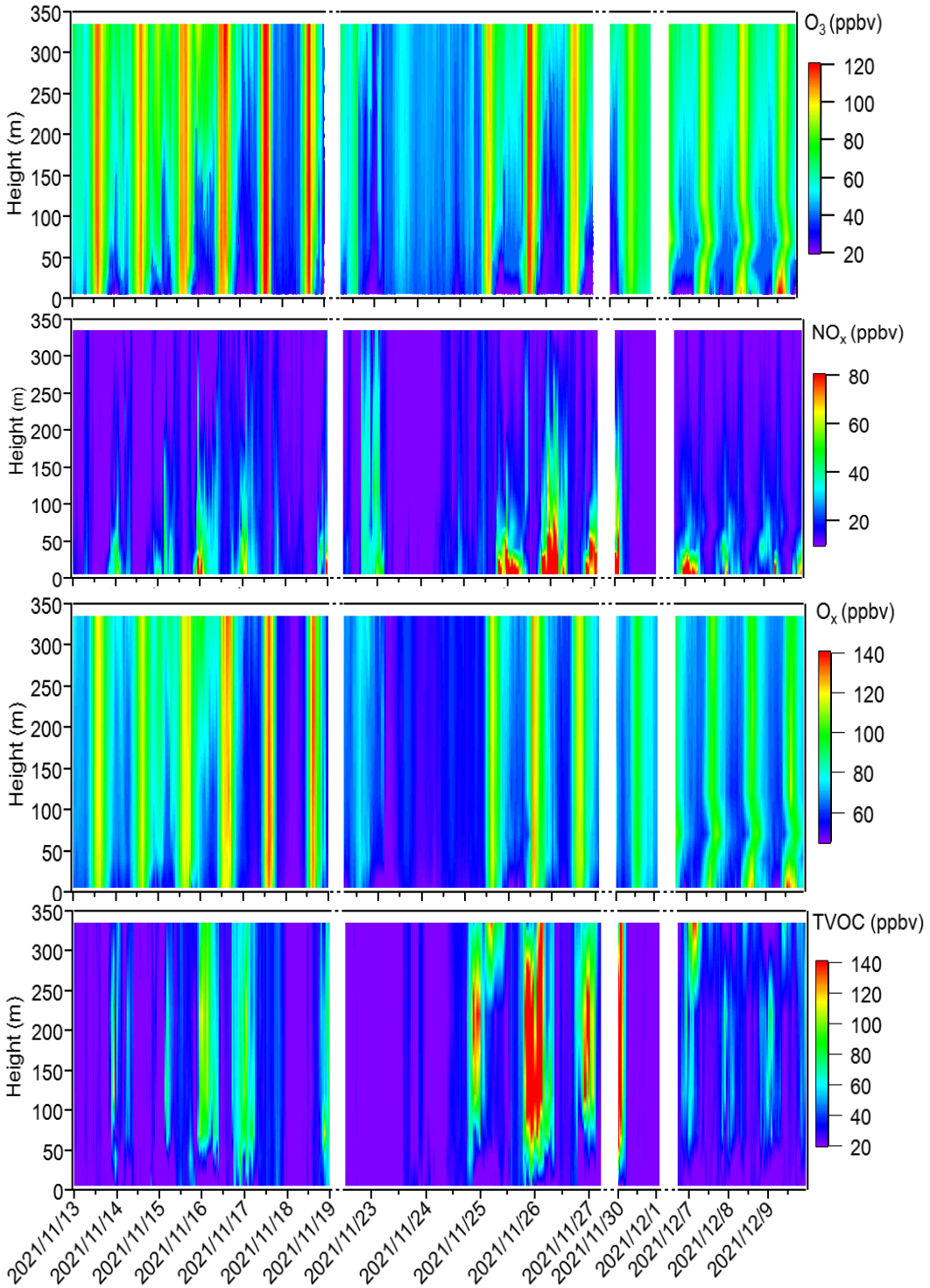

Figure 2. Time series of vertical profiles for O_3, NOx, Ox, and TVOC during the observation period. The contour plots are made using the measured values from six heights.

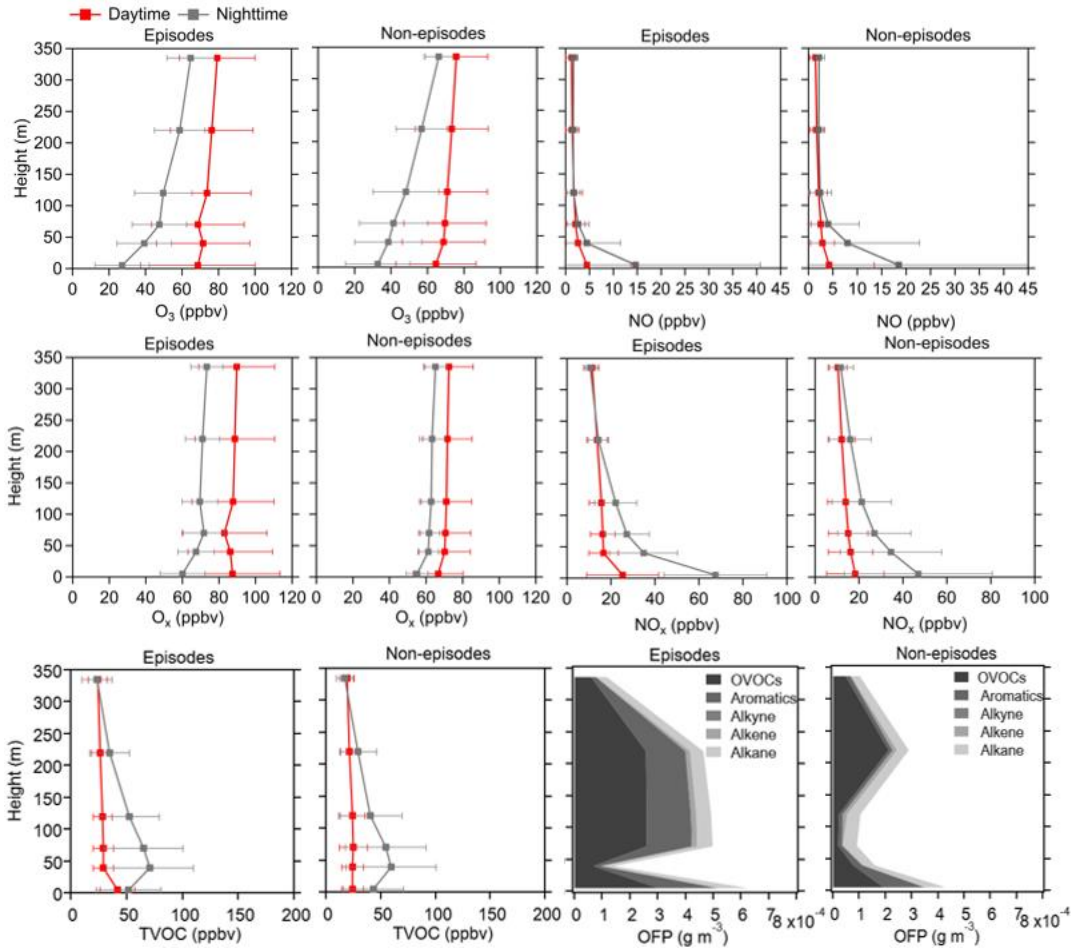

Figure 3. Average vertical profiles of O_3, NO, Ox, NOx, and TVOC during both daytime and nighttime, and OFP of different VOCs types during daytime at six heights (5, 40, 70, 120, 220, and 335 m), including episodes and non-episodes throughout the observation period. The error bars indicate the standard deviation calculated from the measured values during these periods.

3.1.2 Vertical profiles of O_3 and its precursors at 5-335 m level

Figure 2 shows the contour plots illustrating the vertical profiles of O_3, NOx, Ox(=O_3+NO_2), and TVOC. From Fig. 2, minimal vertical gradients were observed during daytime in the concentration of all species–O_3, NOx, Ox, and TVOC–due to the rapid vertical mixing effects. However, distinct vertical gradients were observed during nighttime owing to the stability of the nocturnal residual layer. Elevated concentrations of O_3 and Ox were identified at higher altitudes, whereas higher NOx concentrations predominantly occurred at ground level. We further elucidated the vertical distribution patterns of different pollutants as well as the OFP of different VOCs groups during local daytime (6:00-18:00 LT) and nighttime (19:00-5:00 LT) for both episodes and non-episodes, as shown in Fig. 3.

The vertical profiles of averaged concentrations of various pollutants exhibit similar trends during both episodes and non-episodes, with O_3 showing an increasing trend from 5 m above ground level to 355 m, aligning with findings from previous studies (Zhang et al., 2019; Wang et al., 2021). Given that NOx has a significant titration effect on O_3, the lower O_3 concentration at ground level may be attributed to the increase in NOx concentration (Zhang et al., 2022) and also the dry deposition near the ground (Li et al., 2022). NO and NOx showed an opposite trend compared to O_3. These two factors jointly effected the Ox changing trend with heights, and consequently, the gradients of Ox concentrations showed a weaker increasing trend from the 5 m ground level to 355 m height compared to O_3. This observation demonstrated a more pronounced NO titration effect at the 5 m ground level compared to the effect at 355 m height. However, the TVOC showed variable trends with increased height for daytime and nighttime during episodes and non-episodes. During daytime, TVOC initially decreased from 5 m to 40 m, and then continuously increased from 40 m to 355 m during episodes, while continuously slightly decreased from 5 m to 335 m during non-episodes. During nighttime, TVOC concentrations first increased from 5 m to 40 m and then continuously decreased from 40 m to 335 m during both episodes and non-episodes. We further plotted the OFP of different VOCs categories at various altitudes, including OVOCs, aromatics, alkyne, alkene, and alkane, and found that the total OFP was highest at 5 m ground level and exhibited higher levels during episodes compared to non-episode periods. Subsequently, there was a significant decrease at 40 m height during both episodes and non-episodes. However, there was a sharp increase observed at 70 m, 120 m, and 220 m during episodes, contrasting with a gradual rise during non-episode periods, which eventually reach a peak at 220 m during non-episodes. A consistent decrease of OFP from 220 m to 335 m was observed during both episodes and non-episodes. The OFP was primarily attributed to OVOCs among different VOCs categories at different altitudes throughout both episodes and non-episodes, followed by aromatics and alkane during episodes and non-episodes, respectively.

In conclusion, our daytime observations revealed minimal vertical gradients in the concentrations of O_3, NOx, Ox, and TVOC, attributed to the rapid vertical mixing effects driven by surface heating effects (Tang et al., 2017). This suggests that ground-level O_3 concentrations would be representative of the entire vertical column. Nonetheless, the OFP varies for different VOCs profiles at various heights, and the

vertical mixing effects facilitates the downward transport of O_3 photochemically formed from higher altitudes to the near-ground layer. Consequently, a box model constraining to ground-level NOx and VOCs concentrations may not accurately reflect the in situ O_3 production in the vertical atmospheric column.

3.2 O_3 pollution episodes formation mechanism at near-ground surface

In this section, we first explore the possible reason for O_3 pollution episodes on the 5 m ground level, aiming to identify the contribution of chemical and physical processes to change in O_3 concentrations (Sect. 3.2.1). Subsequently, we assessed the modelling performance and investigated the potential reasons for the modelling bias in photochemical O_3 formation by comparing the measured $P(O_3)_{net}$ with the modelled $P(O_3)_{net}$ (Sect. 3.2.2). To gain insights into the photochemical O_3 formation mechanism at different heights and understand their role in overall O_3 pollution, we further discuss the chemical budget of O_3 at different heights (Sect. 3.2.3), the vertical and temporal variability of $P(O_3)_{net}$ and O_3 formation regime (Sect. 3.2.4), along with potential bias within the modelling approach (Sect. 3.2.5).

3.2.1 Contribution of chemical and physical processes to O_3 changes on the ground level

As concluded in Sect. 3.1.1, O_3 pollution episodes may be jointly affected by the photochemical reactions and physical transport. In order to identify the main reasons for O_3 pollution on the ground level, we calculated the contribution of chemical and physical processes to O_X concentration changes at 5 m ground level separately for all 3 episodes and 2 non-episodes. Typically, as dry deposition contributes a relatively small portion and can often be considered negligible, making vertical and horizontal transport the main contributors to physical processes (Tan et al., 2019).

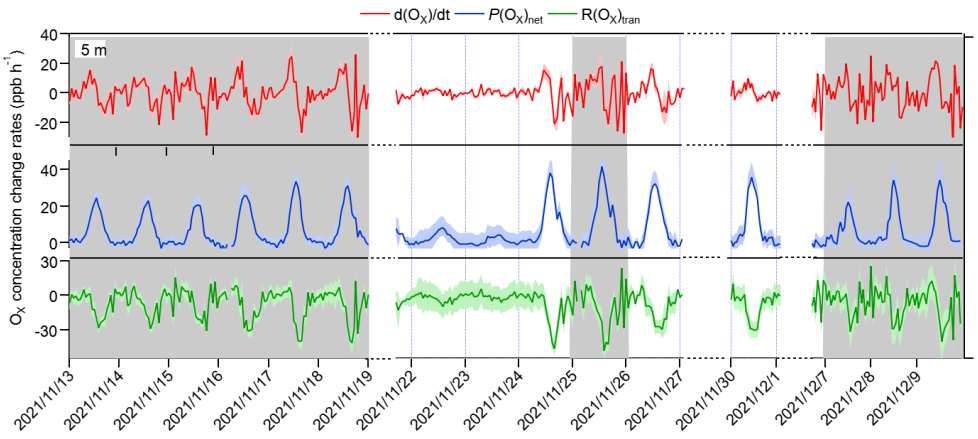

Figure 4. Time series of O_X concentration changes ($d(O_X)/dt$) and contributions from local photochemical production ($P(O_X)_{net}$) and physical transport ($R(O_X)_{tran}$). The shaded areas of $d(O_X)/dt$, $P(O_X)_{net}$, and $R(O_X)_{tran}$ represent one standard deviation (denoted by σ) of the mean $d(O_X)/dt$, the uncertainty of measured $P(O_X)_{net}$, and the propagated error of $R(O_X)_{tran}$, respectively.

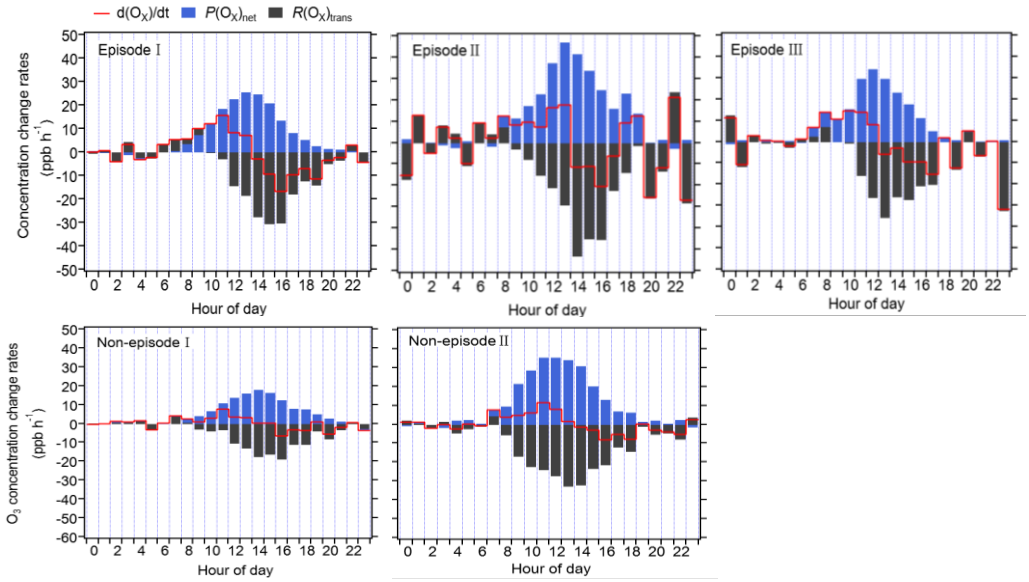

Figure 5. Diurnal variation of the contribution of chemical and physical transport to O_3 changes on the ground level.

$R(O_X)_{trans}$ at 5 m ground level was derived from $\frac{dO_X}{dt}$ minus $P(Ox)_{net}$, according to Eq. (5) shown Sect. 2.3.2, their hourly averages and diurnal variations are shown in Figs. 4 and 5, respectively. From these figures, it is evident that the fluctuation of the O_X concentration change rate ($d(O_X)/dt$) at ground level is typically small and primarily dominated by the physical processes during nighttime. During nighttime, $P(O_X)_{net}$ should be zero without sun radiation, the significant $P(O_X)_{net}$ shown in Fig. 5 may be

due to the measurement uncertainty of $P(O_X)_{net}$, which is determined by the measurement error of O_X of CAPS-NO_2 monitor in the reaction and reference chambers (as discussed in Sect. S4). The measurement uncertainty of $P(O_X)_{net}$ is higher at lower $P(O_X)_{net}$ values (as shown in Fig. 4), which was mainly determined by the instrumental error of O_X measurement and the ambient O_X concentrations during nighttime. It was estimated to be ~ 38 % and can be considered as the measurement precision. Around 6:00-7:00 LT, O_3 concentrations increase for all episodes and non-episodes, mainly due to physical transport during episodes I and II and non-episodes I, while photochemical reactions and physical processes are equally important for episodes III and non-episode II. This could be due to short-term strong vertical turbulence in the early morning, which leads to an expansion of the boundary layer height and makes the residual layer "leaky", allowing vertical transport. At the same time, O_3 precursors were also transported down from the residual layer, and with increasing sunlight, these O_3 precursors underwent rapid photochemical reactions that competed with the physical processes between 6:00-7:00 LT, leading to a sharp increase in $P(O_X)_{net}$ between 8:00 to 12:00 LT. The $P(O_X)_{net}$ peaked around 11:00-14:00 LT and started to decrease around 15:00, eventually approaching zero by around 19:00-20:00 LT. Between 7:00-8:00 LT, $R(O_X)_{tran}>0$ for all episodes and non-episodes, indicating inflow of O_3 from physical transport, increasing surface O_3 concentration by averages of 4.7, 3.9, 2.3, 3.5, and 4.5 ppbv h^{-1} for episodes I, II, III, and non-episodes I and II, respectively. From 9:00 to 10:00 LT, $R(O_X)_{tran}>0$ only for episodes I, increasing the O_3 concentration by 1.5 ppbv h^{-1}, indicating inflow of O_3 from physical transport; on the contrary, $R(O_X)_{tran}<0$ for episodes II and III, and non-episodes I and II, indicating outflow of O_3 from physical transport, decreasing the O_3 concentration by 3.1, 0.1, 3.0, and 16.9 ppbv h^{-1}, respectively. After 10:00 LT, $R(O_X)_{tran}<0$ for all episodes and non-episodes, indicating outflow of O_3 from the observation sites, possibly due to accumulated photochemically formed O_3 increasing the concentration at the observation site, diffusing upward or to surrounding areas.

In conclusion, the observed daytime O_3 concentration changes during all episodes and non-episodes were influenced by both photochemical production and physical transport. In the early morning, the increase in O_3 concentrations can be attributed to photochemical reactions, physical processes, and possibly reduced NO titration effects as the boundary layer height increases. Around noon, O_3 concentrations stabilize,

suggesting a balance between photochemical reactions and physical transport affecting O_3 concentration changes. In the afternoon, O_3 concentrations decrease due to the transport of photochemically formed O_3 from the observation site to upwards or the surrounding areas. Our findings indicate that local photochemical reactions dominate O_3 pollution. For example, O_3 pollution episodes recorded during the observation period manifest under specific conditions: ① high photochemical O_3 production (i.e., episode II); ② moderate photochemical O_3 productions coupled with O_3 accumulation under stable weather conditions (i.e., episodes I and III). In contrast, non-episodes observed during the observation period occur under different conditions: ① low levels of photochemical O_3 production (i.e., non-episodes I); ②elevated photochemical O_3 production, with O_3 transport to surrounding areas under favorable diffusion conditions (i.e., non-episodes II).

3.2.2 The model performance

In order to test the simulation ability of OBM-MCM model for $P(O_3)_{net}$, we compared the measured and modelled $P(O_3)_{net}$ at 5 m ground level, as depicted in Fig. S3a. The measured and modelled $P(O_3)_{net}$ revealed close alignment during episodes I and III, yet displayed discernible variations during episode II, non-episode I, and non-episode II. Assessment metrics including IOA, NMB, and NME were computed based on the observed and modelled $P(O_3)_{net}$ over the entire measurement period (as described in Sect. 2.3.3). The IOA ranged between 0.87 (25^{th} percentile) and 0.90 (75^{th} percentile) for the measured and modelled $P(O_3)_{net}$ across the measurement period, indicating the acceptable performance of the OBM-MCM model simulation (a higher IOA value signifies a stronger agreement between simulated and observed values). Additionally, comparison of measured and modelled O_3 concentrations at different heights (as shown in Fig. S4) revealed generally higher modelled values during daytime and closer alignment during nighttime at lower heights (i.e., 5 m, 40 m, and 70 m), while discrepancies were observed at higher heights (i.e., 120 m, 220 m, and 335 m). These phenomena may be primarily attributed to uncertainties in assumed physical processes in the modelling, such as vertical and horizontal transport. Previous studies have utilized the comparison of measured and modelled O_3 concentrations to determine the dilution factor in modelling studies, discovering that suitable dilution factors vary by location (Yang et al., 2021). To achieve the best agreement between the modelled O_3 concentrations and the observed values, we applied different dilution factors (the

lifetime of the species) in the modelling, varying from 6 h to 24 h. We found that the simulated O_3 is closest to the measured O_3 concentrations when the lifetime of the species is set to 12 h. However, given that O_3 concentrations are affected by physical transport processes, the dilution factor might only represent the outflow of O_3 from the observation site. Therefore, there may be limitations in using this method for precise comparisons. We further compared the measured and modelled $P(O_3)_{net}$ under different dilution factors. The modelled $P(O_3)_{net}$ initially increases and then decreases as the dilution factor decreases (equivalent to an increase of species lifetime). However, the influence of varying dilution rates on the modelled $P(O_3)_{net}$ is minimal, constituting less than 30 %, due to the short lifetimes of the HO_2 and RO_2 radicals, which determine the $P(O_3)_{net}$ values (Wang et al., 2021). Notably, the modelled $P(O_3)_{net}$ closely matched the measured values when the species lifetime was set to12 h, as illustrated in Fig. S3b. Consequently, a constant dilution factor of 1/43200 s^{-1} was applied throughout the observation period. Further investigations revealed an IOA range between 0.80 (25^{th} percentile) and 0.82 (75^{th} percentile) for measured and modelled O_3 concentrations at 5 m ground level, which lies in between the IOA result for the modelled and observed O_3 concentrations in previous studies, which range between 0.68 and 0.89 (Wang et al., 2018), signifying the modelling results for O_3 concentrations here are acceptable. The calculated NMB and NME using the modelled and observed $P(O_3)_{net}$ at 5 m ground level during the whole measurement period ranged from -0.42 (25^{th} percentile) to -0.31 (75^{th} percentile) and -0.42 (25^{th} percentile) to 0.54 (75^{th} percentile), respectively. These analysis results indicate that the model underestimates the measured $P(O_3)_{net}$ by a factor ranging from 1.42 (25^{th} percentile) to 1.31 (75^{th} percentile), calculated as (1+|NMB|), and the simulation results are reliable (with -1<NME<1).

The mean diel variation of measured and modelled $P(O_3)_{net}$ during different episodes and non-episodes are shown in Fig. 6a-e. The maximum daily $P(O_3)_{net}$ values were 29.3, 47.2, and 34.2 ppbv h^{-1} for episodes I, II, and III, and 17.9 and 35.5 ppbv h^{-1} for non-episodes I and II, respectively. These values were comparable to or lower than those measured in urban areas of Houston, United States (40-50 and 100 ppbv h^{-1} in autumn and spring, respectively) (Baier et al., 2015; Ren et al., 2013), but higher than those measured in a remote area of Japan (10.5 ppbv h^{-1} in summer) and an urban area of Pennsyvania, United States (~ 8 ppbv h^{-1} in summer) (Sadanaga et al., 2017; Cazorla and Brune, 2020). The averaged diel profiles of measured and simulated $P(O_3)_{net}$

exhibited large standard deviations (as depicted in Table 1), representing their day-to-day variation throughout the campaign. The measured $P(O_3)_{net}$ were mostly higher than the modelled $P(O_3)_{net}$, which could be attributed to the underestimation of RO_2 under high NO conditions, leading to substantial disparities between calculated $P(O_3)_{net}$ derived from measured and modelled RO_2 concentrations, as highlighted in previous studies (Whalley et al., 2018, 2021; Tan et al., 2017, 2018). The median value of [measured $P(O_3)_{net}$-modelled $P(O_3)_{net}$]/measured $P(O_3)_{net}$ ranged from 22% to 45% for different episodes and non-episodes. To delve deeper, we further investigated the relationship between the daily disparities of measured and modelled $P(O_3)_{net}$ ($\Delta P(O_3)_{net}$ = measured $P(O_3)_{net}$-modelled $P(O_3)_{net}$) and average daytime NO concentrations during different episodes and non-episodes, as depicted in Fig. 6f. The observed elevated $\Delta P(O_3)_{net}$ at higher NO concentrations aligns with findings from previous studies, which suggest that multiple factors could contribute to these outcomes. For example, the reaction of OH with unknown VOCs (Tan et al., 2017), the missing RO_2 production from photolysis $ClNO_2$ (Whalley et al., 2018; Tan et al., 2017), and the underestimation of OVOCs photolysis (Wang et al., 2022b) in modelling approaches may lead to the underestimation of RO_2, thus underestimating the modelled $P(O_3)_{net}$. Further analysis showed that the underestimation of $P(O_3)_{net}$ can lead to the NOx-limited regime being shifted to the VOCs-limited regime, thus underestimating the NOx-limited regime (Wang et al., 2022b, 2024). However, the derived IOA, NMB, and NME values from the modelled and observed $P(O_3)_{net}$ (and O_3) at 5 m ground during different episodes and non-episodes indicate that the model proficiently reproduces the genuine $P(O_3)_{net}$ at the observation site (as shown in Table S3). Consequently, these results provide confidence in exploring the vertical and temporal variations of $P(O_3)_{net}$ and O_3 formation sensitivities utilizing the outcomes from the modelling approach. Nonetheless, it is important to acknowledge and discuss the potential biases caused by the modelling methodology in this study.

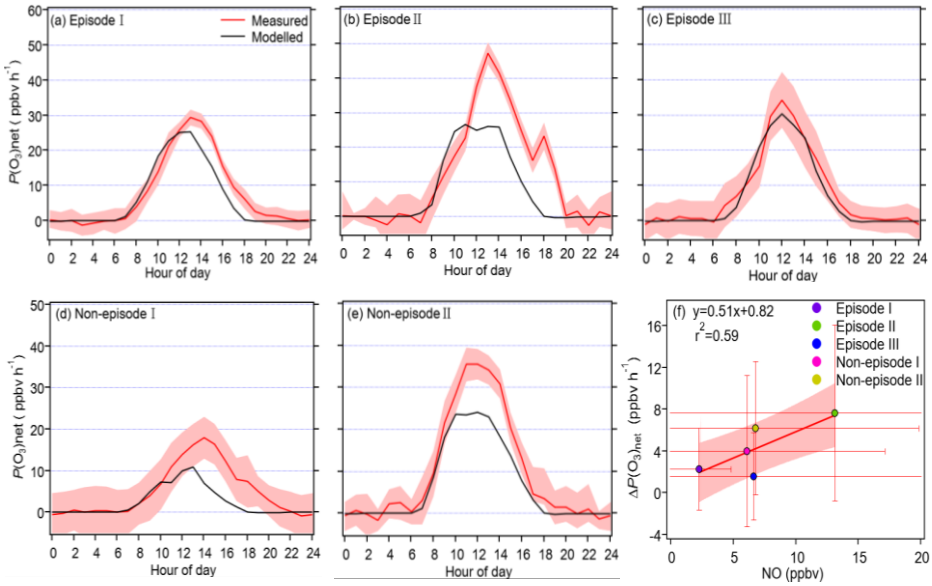

Figure 6. (a-e) diurnal variations of the measured and modelled $P(O_3)_{net}$ during the observation period, and (f) the relationship between the average daily differences of measured and modelled $P(O_3)_{net}$ ($\Delta P(O_3)_{net}$) and the average daytime NO concentrations during different episodes and non-episodes.

3.2.3 Vertical and temporal variability of $P(O_3)_{net}$ budget

The detailed $P(O_3)_{net}$ budget at different heights during the observation period from the modelling results are shown in Fig. 7. Across various heights and different episodes and non-episodes, the contributions of different reaction pathways to $P(O_3)$ were almost the same, with HO_2+NO as the major O_3 production pathway, followed by CH_3O_2+NO and other RO_2+NO, where other RO_2+NO encompasses all RO_2 except CH_3O_2. This result aligns with previous studies (Liu et al., 2021; Liu et al., 2022). The major O_3 destruction pathway was OH+NO_2 (loss of OH radicals), followed by net RO_2+NO_2 (form peroxyacetyl nitrate, commonly called PAN species) and O_3 photolysis, while other O_3 destruction pathways, including O_3+OH, O_3+HO_2, C_5H_8+O_3, C_3H_6+O_3, and C_2H_4+O_3, together contributed negligibly to O_3 destruction. These $P(O_3)$ and $D(O_3)$ reaction pathways occurred between 6:00-18:00 LT, exhibiting strong diurnal variation characterized by a sharp increase between 6:00-11:00 LT in the morning, peaking between 11:00 and 14:00 LT, and decreasing rapidly after 14:00 LT. These phenomena were in accordance with the concentration changes of the major oxidants (i.e., OH, O_3, and NO_3), as shown in Fig. S5, where OH radicals and O_3 concentrations increased significantly in the morning and reached a peak around noon, followed by sharp afternoon decreases.

The diurnal changes in the concentrations of different reaction pathways to $P(O_3)$ and $D(O_3)$ at 5 m ground level during different episodes and non-episodes are depicted in Fig. S6. We note that the maximum total $P(O_3)$ resulting from diel variations at 5 m ground level for episode I, II, and III were 32.0, 34.9, and 38.3 ppbv h^{-1}, respectively. These values were consistently higher than the maximum total $P(O_3)$ observed for non-episodes I and II, which were 15.6 and 30.7 ppbv h^{-1}, respectively. However, as $P(O_3)_{net}$ was determined by both $P(O_3)$ and $D(O_3)$, the maximum total $D(O_3)$ values resulting from diel variations during episodes I, II, III, and non-episode I, II, were 5.0, 5.7, 5.1, 2.4, and 5.3 ppbv h^{-1}, respectively. Consequently, the modelled $P(O_3)_{net}$ during episodes does not exhibit a statistically significant difference from that during non-episodes (Mann-Whitney p value=0.12), as shown in Fig. S5, which is in agreement with the measured $P(O_3)_{net}$ (Mann-Whitney p-value=0.28), as depicted in Sect. 3.1.1.

The diurnal variation of $P(O_3)_{net}$ during different episodes and non-episodes obtained by OBM-MCM modelling at different heights are shown in Fig. 8. We saw that the $P(O_3)_{net}$ all showed a decreasing trend with the increase of the measurement height during different episodes and non-episodes, but the variation of $P(O_3)_{net}$ along with the measurement height differed for different episodes and non-episodes. For example, the decrement of the averaged $P(O_3)_{net}$ during 6:00-18:00 LT from 5 m to 335 m were 1.5 and 0.6 ppbv h^{-1} for episode I and non-episode I, respectively, which was relatively smaller than that during episode II, episode III, and non-episode II, which were 5.3, 5.4, and 4.0 ppbv h^{-1}, respectively. To explore the reason, we plotted the differences of calculated OH reactivities at 5 m and 335 m of different VOCs groups (marked as ΔOH reactivity) as a function of the $P(O_3)_{net}$ change at 5 m and 335 m (marked as $\Delta P(O_3)_{net}$), including nonmethane hydrocarbons (NMHC), anthropogenic volatile organic compounds (AVOC), biogenic volatile organic compounds (BVOC), and oxygenated volatile organic compounds (OVOC) (as shown in Fig.8f). The VOCs species included in each category are listed in Table S2. We found that the OH reactivities of AVOC and OVOC had the highest correlation coefficients (R^2) with the $\Delta P(O_3)_{net}$, which are 0.85 and 0.67, respectively, indicating their predominant influence on the decrement of $P(O_3)_{net}$ from 5 m to 335 m. However, the OH reactivity change from 5 m to 335 m of different groups was quite different. Therefore, we further explored O_3 formation sensitivity to its different VOCs precursors and precursor groups.

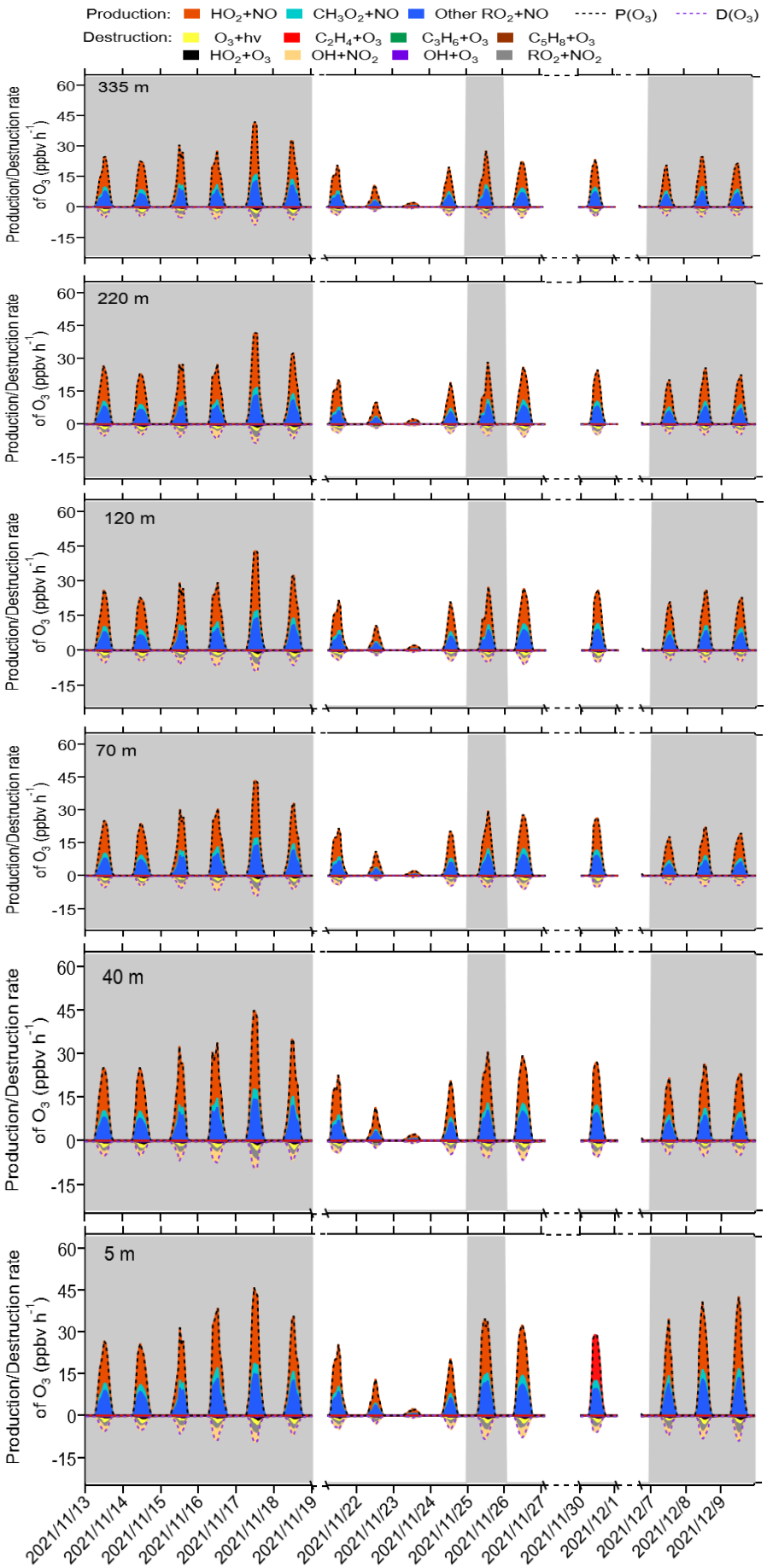

721
722
723
724
725
726
727
728
729
730
731

Figure 7. Time series of model-simulated O_3 production and destruction rates during 13 November and 9 December 2021, at different heights at SZMGT, the gray columns show the typical O_3 episodes that occurred.

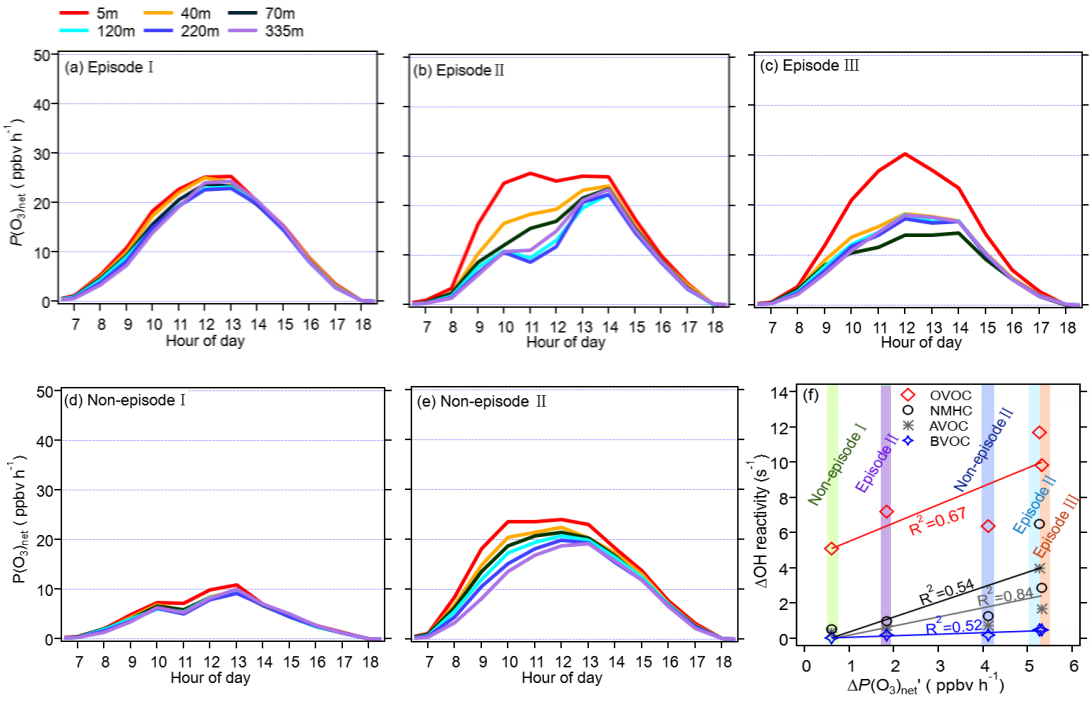

Figure 8. (a-e) Diurnal variation of vertical profile of the model-simulated $P(O_3)_{net}$ during different episodes and non-episodes from 13 November to 9 December 2021, and (f) the relationship between the average daytime differences of modelled $P(O_3)_{net}$ (denoted as $\Delta P(O_3)_{net}$), and OH reactivity of different precursor groups at 5 m and 335 m (denoted as ΔOH reactivity).

3.2.4 Vertical distributions of O_3 formation regime

To investigate the reasons behind the variable distribution of $P(O_3)_{net}$ at varying heights, we clarified the sensitivity of O_3 formation to different O_3 precursors or precursor groups, including NMHC, AVOC, BVOC, OVOC, CO, and NOx, by calculating their RIRs during different episodes and non-episodes, as shown in Fig. 9. The VOCs species, categorized into different precursor groups as listed in Table S2, indicate that some species depicted in Fig. 9 may appear in multiple categories and hence could be repeated. We note that AVOC includes both NMHC and OVOC. Figure 9 demonstrates that the aggregate RIR of OVOC and NMHC is nearly identical to that of AVOC alone. Recognizing that VOC species within the OVOC category are primarily originate from anthropogenic sources, but can also originate from biogenic precursors (Wu et al., 2020; Park et al., 2013), we

acknowledge the possibility of an overestimated RIR for AVOC and due to this overlap. As illustrated in Fig. 9, the RIR values for different O_3-precursors or precursor groups don't exhibit significant variation at different heights during specific episodes or non-episodes, indicating a similar photochemical O_3 formation regime. However, the O_3 formation regimes differ between different episodes or non-episodes. During O_3 polluted episode I, O_3 formation is located in a transition regime and is more sensitive to VOCs emissions. Conversely, during O_3 polluted episodes II and III, and non-episodes I and II, it is located in VOCs sensitive regime. This finding aligns with previous studies suggesting that photochemical O_3 formation in the PRD region is likely VOC-limited or mixed-limited (Hong et al., 2022; Lu et al., 2018). The results suggest complexity of O_3 mitigation at the observation site. For example, during polluted episode I, reducing both VOCs and NOx can mitigate photochemical O_3 formation. However, during other O_3 polluted episodes and non-episodes, reducing VOCs can effectively alleviate photochemical O_3 formation, while reducing NOx might aggravate it. Nevertheless, during all episodes and non-episodes, O_3 formation is most sensitive to AVOC (RIR: 0.83-1.12), followed by OVOC (RIR: 0.59-0.79) at different heights, given that the AVOC includes NMHC and OVOC, there is urgent need to reduce NMHC and OVOC emissions to mitigate O_3 pollution in this area. Additionally, it is evident that OVOCs have a substantially higher RIR than NMHC, therefore, it is more accurate to conclude that the O_3 formation is most sensitive to OVOC rather than AVOC.

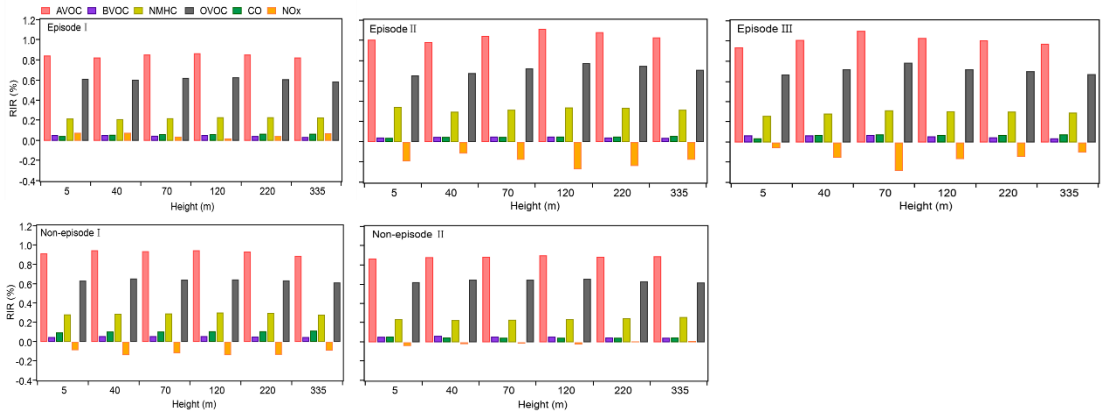

Figure 9. RIR values for O_3-precursor or precursor groups at different heights during different classified episodes.

The RIR tests for different episodes and non-episodes at various hours of the local daytime are illustrated in the Supplement (Fig. S7). The results indicate that the diurnal

changes of RIR values for different episodes and non-episodes exhibit remarkable similarities. In the morning, the RIR values for various VOC groups, including AVOC, BVOC, OVOC, and CO, are typically higher than those for NOx. However, they gradually decrease throughout the day until 16:00 LT, then increase and reach a peak at 18:00 LT. Interestingly, the RIR values at this peak are lower than those at 8:00 LT in the morning. Conversely, the RIR values for NOx are usually around zero or below zero during most of the day, gradually increasing around 16:00 LT and peaking at 18:00 LT. This suggests a transition in the photochemical O_3 formation regime throughout the day, shifting from a VOC-limited regime in the morning to a transition regime and more sensitive to NOx in the afternoon around 16:00 LT. The diurnal variations of the RIRs of different O_3 precursors or precursor groups offer detailed insights into the dominant factors influencing the photochemical formation of O_3 at different times of a day.

Through the sensitivity study, NOx is not found to be the limiting factor affecting $P(O_3)_{net}$, therefore, reactions involving NOx in the ROx radicals cycle, such as $RO_2+NO \rightarrow HO_2$ and $HO_2+NO \rightarrow OH$, should occurred efficiently. Conversely, reactions not involving NOx, such as $OH+VOCs \rightarrow RO_2$, be the limiting steps of the ROx radicals cycling. We further identified and presented the three VOC species with the highest OFP in NMHC and OVOC groups during different episodes and non-episodes in Table S4. Results show that compounds such as toluene, *m/p*-xylene, and n-butane in NMHC group, formaldehyde, hydroxyacetone, and ethanol in OVOC group have identified as the most significant contributors to the total OFP in all episodes and non-episodes. Toluene, *m/p*-xylene, and n-butane are often associated with specific industrial processes (Shi et al., 2022; Liang et al., 2017), while formaldehyde, hydroxyacetone, and acetaldehyde can originate from both the industrial processes and natural sources (Parrish et al., 2012; Fan et al., 2021; Spaulding et al., 2003; Salthammer 2023). Priority should be given to reducing these emission sources in order to mitigate O_3 pollution in the PRD area of China.

4 Conclusions

We carried out a field observation campaign in an urban area in Pearl River Delta (PRD) in China, focusing on investigating the vertical temporal variability of near-surface O_3 production mechanisms by using a newly built vertical observation system

and the observation-based model coupled to the Master Chemical Mechanism (OBM-MCM) v3.3.1. In total, three O_3 pollution episodes and two non-episodes occurred during the observation period. To assess the modelling performance for O_3 production rates and sensitivity, as well as to investigate the potential reasons for O_3 pollution episodes at 5 m ground level, a net photochemical O_3 production rate (NPOPR, $P(O_3)_{net}$) detection system based on the current dual-channel reaction chamber technique was employed to directly measure $P(O_3)_{net}$ at 5 m ground-level.

The vertical profiles of averaged concentrations of various pollutants exhibit similar trends during both episodes and non-episodes. The O_3, NOx, and Ox concentrations show minimal vertical gradient during the daytime due to rapid vertical mixing effects, but distinct vertical gradients emerge during nighttime owing to the stability of the nocturnal residual layer. Higher concentrations of O_3 and Ox were observed at higher heights, while elevated NO and NOx concentrations were mainly detected at ground level. Given that NO has a significant titration effect on O_3, the lower O_3 concentration at ground level may be attributed to the increase in NOx concentration due to a more pronounced NO titration effect, besides the dry deposition near the ground. However, the TVOC and their OFP exhibited variable trends with increased height during both daytime and nighttime, observed in episodes and non-episodes, which indicates the complexities of O_3 formation mechanisms at different heights throughout the atmospheric column. Total OFP was highest at the 5 m ground level and exhibited higher levels during episodes compared to non-episode periods. The OFP was primarily attributed to OVOCs at different altitudes throughout both episodes and non-episodes.

The mean concentrations of O_3 precursors, including CO, NO, NO_2, and TVOC, were not consistently elevated during episodes compared to their levels during non-episodes. By considering the observed O_3 concentrations change and the measured $P(O_3)_{net}$ at 5 m ground level, we found that the O_3 pollution episodes were influenced by both photochemical production and physical transport, with local photochemical reactions playing a key role. O_3 pollution episodes recorded during the observation period occurred under specific conditions: ① high photochemical O_3 productions; ② moderate photochemical O_3 productions coupled with O_3 accumulation under stable weather conditions. The index of agreement (IOA) ranged from 0.87 (25^{th} percentile) to 0.90 (75^{th} percentile) for the measured and modelled $P(O_3)_{net}$ across the measurement

period, indicating the rationality to investigate the vertical and temporal variability of O_3 formation mechanisms using modelling results. However, the measured $P(O_3)_{net}$ generally exceeded the modelled $P(O_3)_{net}$, the differences between measured and modelled $P(O_3)_{net}$ ($\Delta P(O_3)_{net}$) were found to be correlated with NO concentrations. Based on previous studies, this phenomenon could potentially be attributed to the underestimation of RO_2 at high NO conditions, arising from inadequate knowledge concerning photochemical reaction mechanisms. Therefore, the potential biases caused by the modelling methodology were acknowledged and discussed.

From the modelling results, the contribution of different reaction pathways to $P(O_3)$ was almost the same at varying heights during both episodes and non-episodes, with HO_2+NO as the major O_3 production pathway, followed by other RO_2+NO (comprising all RO_2 except CH_3O_2) and CH_3O_2+NO. The major O_3 destruction pathway was OH+NO_2 (loss of OH radicals), followed by net RO_2+NO_2 (forming peroxyacetyl nitrate) and O_3 photolysis. However, other O_3 destruction pathways, including O_3+OH, O_3+HO_2, C_5H_8+O_3, C_3H_6+O_3, and C_2H_4+O_3, collectively contributed negligibly to O_3 destruction. Nevertheless, $P(O_3)_{net}$ showed a decreasing trend with the increase of height during different episodes and non-episodes, which was found mainly attributed to the decline in O_3 precursor concentrations, specifically anthropogenic organic compounds (AVOC) and oxygenated volatile organic compounds (OVOC) groups. We observed that modelling biases were correlated with NO concentrations and VOCs categories, impacting $P(O_3)_{net}$ through the regulation of the RO_2 radicals' budget. The median relative difference between measured and modelled $P(O_3)_{net}$ ranged from 22-45 % during different episodes and non-episodes. Therefore, the variation of $P(O_3)_{net}$ along with the measurement height might be even larger than our initial assessment.

Similar photochemical O_3 formation regimes were observed at different heights during specific episodes or non-episodes, yet they varied between different episodes or non-episodes. O_3 formation was predominantly located at a transition regime and more sensitive to VOCs emissions during O_3-polluted episode I, whereas it shifted to a VOCs-sensitive regime during O_3-polluted episodes II and III, as well as non-episodes I and II. Further analysis revealed a daytime shift in the photochemical O_3 formation regime, transitioning from a VOC-limited regime in the morning to a transition regime more sensitive to NOx round 16:00 LT in the afternoon. However, the underestimation of RO_2 radicals in the modelling, especially at lower heights with higher NO

concentrations, could result in an overestimate of the VOCs-limited regime. This study highlights the need for more precise analysis using direct measurement techniques in future studies. Nonetheless, throughout all episodes and non-episodes, O_3 formation is most sensitive to OVOC at various heights, emphasizing the urgent need to reduce emissions of these compounds and their precursors to mitigate O_3 pollution in this area.

This is the first measurement report of the vertical-temporal of O_3 formation mechanisms near the ground surface. Together with the deliberation of the possible bias on the vertical-temporal profile of O_3 formation rate and sensitivity using modelling studies, this research provides critical foundational insights. The findings provide us in-depth understanding of near-ground vertical variability in O_3 formation mechanisms, which are influenced by the concentrations of VOCs and NOx, and the distinct OFP associated with different VOCs profiles. During daytime, the vertical mixing of air masses is substantially enhanced due to the effect of surface heating. Consequently, photochemically formed O_3 at higher altitudes can be vertically transported downward to the near-ground layer. Under this condition, control strategies for O_3 precursors based on the O_3 formation mechanisms on the ground-level are insufficient. A more comprehensive approach is necessary to effectively address the complexities of O_3 production throughout the atmospheric column. The vertical variability of O_3 formation mechanisms should be taken into account when making effective O_3 control strategies in the PRD area of China.

Data availability. Data related to this article are available online *at* https://zenodo.org/records/10473104.

Author contributions. BY, JZ, XBL, and MS designed the experiment, YXH and JZ performed the $P(O_3)_{net}$ measurement, BY and XBL built the vertical observation system based on SZMGT. JZ, CZ, AL, BY, JPZ, YXH, YW, XBL, XJH, XS, YC, SY, SY, YW, JPQ collected and analysed the data. JZ wrote the manuscript, all authors revised the manuscript.

Competing interests. The authors declare that they have no known competing interests.

Acknowledgements. This study was funded by the Key-Area Research and Development Program of Guangdong Province (grant no. 2020B1111360003), the Natural Science Foundation of Guangdong Province (grant no. 2024A1515011494),

and the National Natural Science Foundation of China (No. 42305096).

References

Anenberg, S. C., Schwartz, J., Shindell, D., Amann, M., Faluvegi, G., Klimont, Z., Janssens-Maenhout, G., Pozzoli, L., Van Dingenen, R., Vignati, E., Emberson, L., Muller, N. Z., West, J. J., Williams, M., Demkine, V., Hicks, W. K., Kuylenstierna, J., Raes, F., and Ramanathan, V.: Global air quality and health co-benefits of mitigating near-term climate change through methane and black carbon emission controls, Environ. Health. Perspect., 120, 831-839, 10.1289/ehp.1104301, 2012.

Baier, B. C., Brune, W. H., Lefer, B. L., Miller, D. O., and Martins, D. K.: Direct ozone production rate measurements and their use in assessing ozone source and receptor regions for Houston in 2013, Atmos. Environ., 114, 83-91, 10.1016/j.atmosenv.2015.05.033, 2015.

Benish, S. E., He, H., Ren, X., Roberts, S. J., Salawitch, R. J., Li, Z., Wang, F., Wang, Y., Zhang, F., Shao, M., Lu, S., and Dickerson, R. R.: Measurement report: Aircraft observations of ozone, nitrogen oxides, and volatile organic compounds over Hebei Province, China, Atmos. Chem. Phys., 20, 14523-14545, 10.5194/acp-20-14523-2020, 2020.

Carter, W. P. L. and Heo G. (2012): Development of revised SAPRC aromatics mechanisms, Report to the California Air Resources Board Contracts No. 07-730 and 08-326, April 12, 2012. Available at: http://www.cert.ucr.edu/~carter/absts.htm#saprc11, 2012.

Cazorla, M. and Brune, W. H.: Measurement of ozone production sensor, Atmos. Meas. Tech., 3, 545-555, 10.5194/amt-3-545-2010, 2010.

Decker, Z. C. J., Zarzana, K. J., Coggon, M., Min, K.-E., Pollack, I., Ryerson, T. B., Peischl, J., Edwards, P., Dubé, W. P., Markovic, M. Z., Roberts, J. M., Veres, P. R., Graus, M., Warneke, C., de Gouw, J., Hatch, L. E., Barsanti, K. C., and Brown, S. S.: Nighttime chemical transformation in biomass burning plumes: a box model analysis initialized with aircraft observations, Environ. Sci. Technol., 53, 2529-2538, 10.1021/acs.est.8b05359, 2019.

Fan, J., Ju, T., Wang, Q., Gao, H., Huang, R., and Duan, J.: Spatiotemporal

939 variations and potential sources of tropospheric formaldehyde over eastern China based
940 on OMI satellite data, Atmos. Pollut. Res., 12, 272-285, 10.1016/j.apr.2020.09.011,
941 2021.

942 Fiore, A. M., Dentener, F. J., Wild, O., Cuvelier, C., Schultz, M. G., Hess, P.,
943 Textor, C., Schulz, M., Doherty, R. M., Horowitz, L. W., MacKenzie, I. A., Sanderson,
944 M. G., Shindell, D. T., Stevenson, D. S., Szopa, S., Van Dingenen, R., Zeng, G.,
945 Atherton, C., Bergmann, D., Bey, I., Carmichael, G., Collins, W. J., Duncan, B. N.,
946 Faluvegi, G., Folberth, G., Gauss, M., Gong, S., Hauglustaine, D., Holloway, T.,
947 Isaksen, I. S. A., Jacob, D. J., Jonson, J. E., Kaminski, J. W., Keating, T. J., Lupu, A.,
948 Marmer, E., Montanaro, V., Park, R. J., Pitari, G., Pringle, K. J., Pyle, J. A., Schroeder,
949 S., Vivanco, M. G., Wind, P., Wojcik, G., Wu, S., and Zuber, A.: Multimodel estimates
950 of intercontinental source-receptor relationships for ozone pollution, J. Geophys. Res.,
951 114, 10.1029/2008jd010816, 2009.

952 Geng, C., Wang, J., Yin, B., Zhao, R., Li, P., Yang, W., Xiao, Z., Li, S., Li, K.,
953 and Bai, Z.: Vertical distribution of volatile organic compounds conducted by tethered
954 balloon in the Beijing-Tianjin-Hebei region of China, J. Environ. Sci., 95, 121-129,
955 10.1016/j.jes.2020.03.026, 2020.

956 Hao, Y., Zhou, J., Zhou, J. P., Wang, Y., Yang, S., Huangfu, Y., Li, X. B., Zhang,
957 C., Liu, A., Wu, Y., Zhou, Y., Yang, S., Peng, Y., Qi, J., He, X., Song, X., Chen, Y.,
958 Yuan, B., and Shao, M.: Measuring and modeling investigation of the net
959 photochemical ozone production rate via an improved dual-channel reaction chamber
960 technique, Atmos. Chem. Phys., 23, 9891-9910, 10.5194/acp-23-9891-2023, 2023.

961 Hong, Q., Zhu, L., Xing, C., Hu, Q., Lin, H., Zhang, C., Zhao, C., Liu, T., Su, W.,
962 and Liu, C.: Inferring vertical variability and diurnal evolution of O_3 formation
963 sensitivity based on the vertical distribution of summertime HCHO and NO_2 in
964 Guangzhou, China, Sci. Total Environ., 827, 10.1016/j.scitotenv.2022.154045, 2022.

965 Jenkin, M. E., Young, J. C., and Rickard, A. R.: The MCM v3.3.1 degradation
966 scheme for isoprene, Atmos. Chem. Phys., 15, 11433-11459, 10.5194/acp-15-11433-
967 2015, 2015.

968 Klein, A., Ravetta, F., Thomas, J. L., Ancellet, G., Augustin, P., Wilson, R.,
969 Dieudonné, E., Fourmentin, M., Delbarre, H., and Pelon, J.: Influence of vertical mixing

and nighttime transport on surface ozone variability in the morning in Paris and the surrounding region, Atmos. Environ., 197, 92-102, 10.1016/j.atmosenv.2018.10.009, 2019.

Li, X.-B., Yuan, B., Wang, S., Wang, C., Lan, J., Liu, Z., Song, Y., He, X., Huangfu, Y., Pei, C., Cheng, P., Yang, S., Qi, J., Wu, C., Huang, S., You, Y., Chang, M., Zheng, H., Yang, W., Wang, X., and Shao, M.: Variations and sources of volatile organic compounds (VOCs) in urban region: insights from measurements on a tall tower, Atmos. Chem. Phys., 22, 10567-10587, 10.5194/acp-22-10567-2022, 2022.

Li, X.-B., Zhang, C., Liu, A., Yuan, B., Yang, H., Liu, C., Wang, S., Huangfu, Y., Qi, J., Liu, Z., He, X., Song, X., Chen, Y., Peng, Y., Zhang, X., Zheng, E., Yang, L., Yang, Q., Qin, G., Zhou, J., and Shao, M.: Assessment of long tubing in measuring atmospheric trace gases: applications on tall towers, Environ. Sci.: Atmos., 3, 506-520, 10.1039/d2ea00110a, 2023.

Li, Y., Liu, B., Ye, J., Jia, T., Khuzestani, R. B., Sun, J. Y., Cheng, X., Zheng, Y., Li, X., Wu, C., Xin, J., Wu, Z., Tomoto, M. A., McKinney, K. A., Martin, S. T., Li, Y. J., and Chen, Q.: Unmanned aerial vehicle measurements of volatile organic compounds over a subtropical forest in China and implications for emission heterogeneity, ACS. Earth. Space. Chem., 5, 247-256, 10.1021/acsearthspacechem.0c00271, 2021.

Liang, X., Chen, X., Zhang, J., Shi, T., Sun, X., Fan, L., Wang, L., and Ye, D.: Reactivity-based industrial volatile organic compounds emission inventory and its implications for ozone control strategies in China, Atmos. Environ., 162, 115-126, 10.1016/j.atmosenv.2017.04.036, 2017.

Liu, J., Liu, Z., Ma, Z., Yang, S., Yao, D., Zhao, S., Hu, B., Tang, G., Sun, J., Cheng, M., Xu, Z., and Wang, Y.: Detailed budget analysis of HONO in Beijing, China: Implication on atmosphere oxidation capacity in polluted megacity, Atmos. Environ., 244, 117957, 10.1016/j.atmosenv.2020.117957, 2021.

Liu, T., Hong, Y., Li, M., Xu, L., Chen, J., Bian, Y., Yang, C., Dan, Y., Zhang, Y., Xue, L., Zhao, M., Huang, Z., and Wang, H.: Atmospheric oxidation capacity and ozone pollution mechanism in a coastal city of southeastern China: analysis of a typical photochemical episode by an observation-based model, Atmos. Chem. Phys., 22, 2173-

2190, 10.5194/acp-22-2173-2022, 2022.

Liu, X., Wang, N., Lyu, X., Zeren, Y., Jiang, F., Wang, X., Zou, S., Ling, Z., and Guo, H.: Photochemistry of ozone pollution in autumn in Pearl River Estuary, South China, Sci. Total Environ., 754, 141812, 10.1016/j.scitotenv.2020.141812, 2021.

Liu, Z., Zha, F., Wang, Y., Yuan, B., Liu, B., and Tang, G.: Vertical evolution of the concentrations and sources of volatile organic compounds in the lower boundary layer in urban Beijing in summer, Chemosphere, 332, 138767, 10.1016/j.chemosphere.2023.138767, 2023.

Lu, X., Hong, J., Zhang, L., Cooper, O. R., Schultz, M. G., Xu, X., Wang, T., Gao, M., Zhao, Y., and Zhang, Y.: Severe surface ozone pollution in China: a global perspective, Environ. Sci. Technol. Lett., 5, 487-494, 10.1021/acs.estlett.8b00366, 2018.

Luo, Y., Dou, K., Fan, G., Huang, S., Si, F., Zhou, H., Wang, Y., Pei, C., Tang, F., Yang, D., Xi, L., Yang, T., Zhang, T., and Liu, W.: Vertical distributions of tropospheric formaldehyde, nitrogen dioxide, ozone and aerosol in southern China by ground-based MAX-DOAS and LIDAR measurements during PRIDE-GBA 2018 campaign, Atmos. Environ., 226, 10.1016/j.atmosenv.2020.117384, 2020a.

Luo, Y. P., Fu, J. Y., Li, Q. S., Chan, P. W., and He, Y. C.: Observation of Typhoon Hato based on the 356-m high meteorological gradient tower at Shenzhen, J. Wind. Eng. Ind. Aerodyn., 207, 104408, 10.1016/j.jweia.2020.104408, 2020b.

Mao, J., Yan, F., Zheng, L., You, Y., Wang, W., Jia, S., Liao, W., Wang, X., and Chen, W.: Ozone control strategies for local formation- and regional transport-dominant scenarios in a manufacturing city in southern China, Sci. Total Environ., 813, 10.1016/j.scitotenv.2021.151883, 2022.

Mousavinezhad, S., Choi, Y., Pouyaei, A., Ghahremanloo, M., and Nelson, D. L.: A comprehensive investigation of surface ozone pollution in China, 2015–2019: Separating the contributions from meteorology and precursor emissions, Atmos. Res., 257, 10.1016/j.atmosres.2021.105599, 2021.

Pan, X., Kanaya, Y., Tanimoto, H., Inomata, S., Wang, Z., Kudo, S., and Uno, I.: Examining the major contributors of ozone pollution in a rural area of the Yangtze

River Delta region during harvest season, Atmos. Chem. Phys., 15, 6101–6111, 10.5194/acp-15-6101-2015, 2015.

Parrish, D. D., Ryerson, T. B., Mellqvist, J., Johansson, J., Fried, A., Richter, D., Walega, J. G., Washenfelder, R. A., de Gouw, J. A., Peischl, J., Aikin, K. C., McKeen, S. A., Frost, G. J., Fehsenfeld, F. C., and Herndon, S. C.: Primary and secondary sources of formaldehyde in urban atmospheres: Houston Texas region, Atmos. Chem. Phys., 12, 3273-3288, 10.5194/acp-12-3273-2012, 2012.

Sadanaga, Y., Kawasaki, S., Tanaka, Y., Kajii, Y., and Bandow, H.: New system for measuring the photochemical ozone production rate in the atmosphere, Environ. Sci. Technol., 51, 2871-2878, 10.1021/acs.est.6b04639, 2017.

Salthammer, T.: Acetaldehyde in the indoor environment, Environ. Sci. Atmos., 3, 474-493, 10.1039/D2EA00146B, 2023.

Shen, H., Liu, Y., Zhao, M., Li, J., Zhang, Y., Yang, J., Jiang, Y., Chen, T., Chen, M., Huang, X., Li, C., Guo, D., Sun, X., Xue, L., and Wang, W.: Significance of carbonyl compounds to photochemical ozone formation in a coastal city (Shantou) in eastern China, Sci. Total Environ., 764, 10.1016/j.scitotenv.2020.144031, 2021.

Shi, J., Bao, Y., Ren, L., Chen, Y., Bai, Z., and Han, X.: Mass concentration, source and health risk assessment of volatile organic compounds in nine cities of Northeast China, Int. J. Environ. Res. Public Health, 19, 4915, 10.3390/ijerph19084915, 2022.

Spaulding, R. S., Schade, G. W., Goldstein, A. H., and Charles, M. J.: Characterization of secondary atmospheric photooxidation products: Evidence for biogenic and anthropogenic sources, J. Geophys. Res., 108, 4247, 10.1029/2002JD002478, 2003.

Sillman, S.: The relation between ozone, NOx and hydrocarbons in urban and polluted rural environments, Atmos. Environ., 33, 1821-1845, 10.1016/S1352-2310(98)00345-8, 1999.

Sklaveniti, S., Locoge, N., Stevens, P. S., Wood, E., Kundu, S., and Dusanter, S.: Development of an instrument for direct ozone production rate measurements: measurement reliability and current limitations, Atmos. Meas. Tech., 11, 741-761,

10.5194/amt-11-741-2018, 2018.

Steinfeld, J. I.: Atmospheric chemistry and physics: from air pollution to climate change, Environ. Sci. Policy. Sustain. Dev., 40, 26-26, 10.1080/00139157.1999.10544295, 1998.

Park, J. H., Goldstein, A. H., Timkovsky, J., Fares, S., Weber, R., Karlik, J., and Holzinger, R.: Active atmosphere-ecosystem exchange of the vast majority of detected volatile organic compounds, Science, 341, 643–647, 10.1126/science.1235053, 2013.

Tan, Z., Lu, K., Jiang, M., Su, R., Wang, H., Lou, S., Fu, Q., Zhai, C., Tan, Q., Yue, D., Chen, D., Wang, Z., Xie, S., Zeng, L., and Zhang, Y.: Daytime atmospheric oxidation capacity in four Chinese megacities during the photochemically polluted season: a case study based on box model simulation, Atmos. Chem. Phys., 19, 3493-3513, 10.5194/acp-19-3493-2019, 2019.

Tan, Z., Lu, K., Dong, H., Hu, M., Li, X., Liu, Y., Lu, S., Shao, M., Su, R., Wang, H., Wu, Y., Wahner, A., and Zhang, Y.: Explicit diagnosis of the local ozone production rate and the ozone-NOx-VOC sensitivities, Sci. Bull., 63(16):1067-1076, 10.1016/j.scib.2018.07.001, 2018.

Tan, Z., Fuchs, H., Lu, K., Hofzumahaus, A., Bohn, B., Broch, S., Dong, H., Gomm, S., Häseler, R., He, L., Holland, F., Li, X., Liu, Y., Lu, S., Rohrer, F., Shao, M., Wang, B., Wang, M., Wu, Y., Zeng, L., Zhang, Y., Wahner, A., and Zhang, Y.: Radical chemistry at a rural site (Wangdu) in the North China Plain: observation and model calculations of OH, HO_2 and RO_2 radicals, Atmos. Chem. Phys., 17, 663-690, 10.5194/acp-17-663-2017, 2017.

Tang, G., Zhu, X., Xin, J., Hu, B., Song, T., Sun, Y., Zhang, J., Wang, L., Cheng, M., Chao, N., Kong, L., Li, X., and Wang, Y.: Modelling study of boundary-layer ozone over northern China - Part I: Ozone budget in summer, Atmos. Res., 187, 128-137, 10.1016/j.atmosres.2016.10.017, 2017.

Wang, C., Yuan, B., Wu, C., Wang, S., Qi, J., Wang, B., Wang, Z., Hu, W., Chen, W., Ye, C., Wang, W., Sun, Y., Wang, C., Huang, S., Song, W., Wang, X., Yang, S., Zhang, S., Xu, W., Ma, N., Zhang, Z., Jiang, B., Su, H., Cheng, Y., Wang, X., and Shao, M.: Measurements of higher alkanes using NO^+ chemical ionization in PTR-ToF-MS: important contributions of higher alkanes to secondary organic aerosols in China,

Atmos. Chem. Phys., 20, 14123–14138, 10.5194/acp-20-14123- 2020, 2020.

Wang, N., Lyu, X., Deng, X., Huang, X., Jiang, F., and Ding, A.: Aggravating O_3 pollution due to NOx emission control in eastern China, Sci. Total Environ., 677, 732-744, 10.1016/j.scitotenv.2019.04.388, 2019.

Wang, P., Chen, Y., Hu, J., Zhang, H., and Ying, Q.: Attribution of tropospheric ozone to NOx and VOC Emissions: considering ozone formation in the transition regime, Environ. Sci. Technol., 53, 1404-1412, 10.1021/acs.est.8b05981, 2019.

Wang, Y., Zhang, Y., Hao, J., and Luo, M.: Seasonal and spatial variability of surface ozone over China: contributions from background and domestic pollution, Atmos. Chem. Phys., 11, 3511-3525, 10.5194/acp-11-3511-2011, 2011.

Wang, W., Parrish, D. D., Wang, S., Bao, F., Ni, R., Li, X., Yang, S., Wang, H., Cheng, Y., and Su, H.: Long-term trend of ozone pollution in China during 2014–2020: distinct seasonal and spatial characteristics and ozone sensitivity, Atmos. Chem. Phys., 22, 8935-8949, 10.5194/acp-22-8935-2022, 2022a.

Wang, W., Yuan, B., Peng, Y., Su, H., Cheng, Y., Yang, S., Wu, C., Qi, J., Bao, F., Huangfu, Y., Wang, C., Ye, C., Wang, Z., Wang, B., Wang, X., Song, W., Hu, W., Cheng, P., Zhu, M., Zheng, J., and Shao, M.: Direct observations indicate photodegradable oxygenated volatile organic compounds (OVOCs) as larger contributors to radicals and ozone production in the atmosphere, Atmos. Chem. Phys., 22, 4117-4128, 10.5194/acp-22-4117-2022, 2022b.

Wang, W.; Yuan, B.; Su, H.; Cheng, Y.; Qi, J.; Wang, S.; Song, W.; Wang, X.; Xue, C.; Ma, C.; Bao, F.; Wang, H.; Lou, S.; Shao, M.: A large role of missing volatile organic compound reactivity from anthropogenic emissions in ozone pollution regulation, Atmos. Chem. Phys., 24, (7), 4017-4027,10.5194/acp-24-4017-2024, 2024.

Wang, X., Zhang, T., Xiang, Y., Lv, L., Fan, G., and Ou, J.: Investigation of atmospheric ozone during summer and autumn in Guangdong Province with a lidar network, Sci. Total Environ., 751, 10.1016/j.scitotenv.2020.141740, 2021.

Wang, Y., Guo, H., Zou, S., Lyu, X., Ling, Z., Cheng, H., and Zeren, Y.: Surface O_3 photochemistry over the South China Sea: Application of a near-explicit chemical mechanism box model, Environ. Pollut., 234, 155-166, 10.1016/j.envpol.2017.11.001,

2018.

Whalley, L. K., Stone, D., Dunmore, R., Hamilton, J., Hopkins, J. R., Lee, J. D., Lewis, A. C., Williams, P., Kleffmann, J., Laufs, S., Woodward-Massey, R., and Heard, D. E.: Understanding in situ ozone production in the summertime through radical observations and modelling studies during the Clean air for London project (ClearfLo), Atmos. Chem. Phys., 18, 2547-2571, 10.5194/acp-18-2547-2018, 2018.

Whalley, L. K., Slater, E. J., Woodward-Massey, R., Ye, C., Lee, J. D., Squires, F., Hopkins, J. R., Dunmore, R. E., Shaw, M., Hamilton, J. F., Lewis, A. C., Mehra, A., Worrall, S. D., Bacak, A., Bannan, T. J., Coe, H., Percival, C. J., Ouyang, B., Jones, R. L., Crilley, L. R., Kramer, L. J., Bloss, W. J., Vu, T., Kotthaus, S., Grimmond, S., Sun, Y., Xu, W., Yue, S., Ren, L., Acton, W. J. F., Hewitt, C. N., Wang, X., Fu, P., and Heard, D. E.: Evaluating the sensitivity of radical chemistry and ozone formation to ambient VOCs and NOx in Beijing, Atmos. Chem. Phys., 21, 2125-2147, 10.5194/acp-21-2125-2021, 2021.

Wolfe, G. M., Marvin, M. R., Roberts, S. J., Travis, K. R., and Liao, J.: The Framework for 0-D Atmospheric Modeling (F0AM) v3.1, Geosci. Model. Dev., 9, 3309-3319, 10.5194/gmd-9-3309-2016, 2016.

World Meteorological Organization, Greenhouse Gas Bulletin No. 18, 2022, https://library.wmo.int/idurl/4/59137.

Wu, C., Wang, C., Wang, S., Wang, W., Yuan, B., Qi, J., Wang, B., Wang, H., Wang, C., Song, W., Wang, X., Hu, W., Lou, S., Ye, C., Peng, Y., Wang, Z., Huangfu, Y., Xie, Y., Zhu, M., Zheng, J., Wang, X., Jiang, B., Zhang, Z., and Shao, M.: Measurement report: Important contributions of oxygenated compounds to emissions and chemistry of volatile organic compounds in urban air, Atmos. Chem. Phys., 20, 14769–14785, 10.5194/acp-20-14769-2020, 2020.

Xue, L. K., Wang, T., Gao, J., Ding, A. J., Zhou, X. H., Blake, D. R., Wang, X. F., Saunders, S. M., Fan, S. J., Zuo, H. C., Zhang, Q. Z., and Wang, W. X.: Ground-level ozone in four Chinese cities: precursors, regional transport and heterogeneous processes, Atmos. Chem. Phys., 14, 13175-13188, 10.5194/acp-14-13175-2014, 2014.

Yang, S., Yuan, B., Peng, Y., Huang, S., Chen, W., Hu, W., Pei, C., Zhou, J., Parrish, D. D., Wang, W., He, X., Cheng, C., Li, X. B., Yang, X., Song, Y., Wang, H.,

Qi, J., Wang, B., Wang, C., Wang, C., Wang, Z., Li, T., Zheng, E., Wang, S., Wu, C., Cai, M., Ye, C., Song, W., Cheng, P., Chen, D., Wang, X., Zhang, Z., Wang, X., Zheng, J., and Shao, M.: The formation and mitigation of nitrate pollution: comparison between urban and suburban environments, Atmos. Chem. Phys., 22, 4539-4556, 10.5194/acp-22-4539-2022, 2022.

Yang, W., Chen, H., Wang, W., Wu, J., Li, J., Wang, Z., Zheng, J., and Chen, D.: Modeling study of ozone source apportionment over the Pearl River Delta in 2015, Environ. Pollut., 253, 393-402, 10.1016/j.envpol.2019.06.091, 2019.

Yuan, B., Chen, W., Shao, M., Wang, M., Lu, S., Wang, B., Liu, Y., Chang, C.-C., and Wang, B.: Measurements of ambient hydrocarbons and carbonyls in the Pearl River Delta (PRD), China, Atmos. Res., 116, 93-104, 10.1016/j.atmosres.2012.03.006, 2012.

Yuan, B., Koss, A. R., Warneke, C., Coggon, M., Sekimoto, K., and de Gouw, J. A.: Proton-Transfer-Reaction Mass Spectrometry: applications in atmospheric sciences, Chem. Rev., 117, 13187–13229, 10.1021/acs.chemrev.7b00325, 2017.

Zhao, W., Tang, G., Yu, H., Yang, Y., Wang, Y., Wang, L., An, J., Gao, W., Hu, B., Cheng, M., An, X., Li, X., and Wang, Y.: Evolution of boundary layer ozone in Shijiazhuang, a suburban site on the North China Plain, J. Environ. Sci., 83, 152-160, 10.1016/j.jes.2019.02.016, 2019.

Zhang, X., Xu, J., Kang, S., Zhang, Q., and Sun, J.: Chemical characterization and sources of submicron aerosols in the northeastern Qinghai–Tibet Plateau: insights from high-resolution mass spectrometry, Atmos. Chem. Phys., 19, 7897-7911, 10.5194/acp-19-7897-2019, 2019.

Zhang, Y., Zhang, Y., Liu, Z., Bi, S., and Zheng, Y.: Analysis of vertical distribution changes and influencing factors of tropospheric ozone in China from 2005 to 2020 based on multi-source data, Int. J. Environ. Res. Public Health, 19, 10.3390/ijerph191912653, 2022.

Zhou, J.; Wang, W.; Wu, Y.; Zhang, C.; Liu, A.; Hao, Y.; Li, X.-B.; Shao, M.: Development and application of a nitrogen oxides analyzer based on the cavity attenuated phase shift technique, J. Environ. Sci., 150, 692-703, 10.1016/j.jes.2023.11.017, 2025.

Zhou, J., Yuan, B., Li, X., and Shao, M.: Measurement and modelling results of O_3 and its precursors [Data set]. Zenodo. 10.5281/zenodo.7854639, 2023.

Zhu, H., Wang, H., Jing, S., Wang, Y., Cheng, T., Tao, S., Lou, S., Qiao, L., Li, L., and Chen, J.: Characteristics and sources of atmospheric volatile organic compounds (VOCs) along the mid-lower Yangtze River in China, Atmos. Environ., 190, 232-240, 10.1016/j.atmosenv.2018.07.026 2018.

Zhu, J., Wang, S., Wang, H., Jing, S., Lou, S., Saiz-Lopez, A., and Zhou, B.: Observationally constrained modeling of atmospheric oxidation capacity and photochemical reactivity in Shanghai, China, Atmos. Chem. Phys., 20, 1217-1232, 10.5194/acp-20-1217-2020, 2020.